POLITECNICO DI TORINO

Master of Science's Degree
in Environmental and Land Engineering

Hollow and solid silica nanoparticles for environmental applications: characterization and transport in porous media

ADVISOR:
Prof. Tiziana Anna Elisabetta Tosco

CO-ADVISOR:
Prof. Subhasis Ghoshal

CANDIDATE:
Alessandro Bosi

Contents

List of Figures

List of Tables

Nomenclature

Greek Symbols

α	Attachment efficiency
α_x	Porous medium dispersivity in flow direction [L]
β_a	Attachment exponent in transient ionic strength conditions
β_d	Detachment exponent in transient ionic strength conditions
β_s	Blocking exponent in transient ionic strength conditions
β_{str}	Straining exponent
γ_s	Blocking multiplier in transient ionic strength conditions [L^3 M^{-1}]
δ_i	Refractive index of i-th medium
ε_0	Vacuum dielectric constant [I^2 t^4 M^{-1} L^{-3}]
$\varepsilon_{r,i}$	Relative dielectric constant of i-th medium
ζ	Absorbivity coefficient [M^{-1} L^2]
η	Single collector removal efficiency
η_D	Single collector contact efficiency due to diffusion
η_G	Single collector contact efficiency due to gravity
η_I	Single collector contact efficiency due to interception
η_0	Single collector contact efficiency
λ	Characteristic wavelength of Van der Waals interaction [L]
μ	Fluid viscosity [M t^{-1} L^{-1}]
ν_e	Electronic absorption frequency in the UV region [t^{-1}]
ρ_b	Porous medium bulk density [M L^{-3}]
ρ_f	Fluid density [M L^{-3}]
ρ_p	Particle density [M L^{-3}]
Φ_{min}	Depth of DLVO primary minimum [M L^2 t^{-2}]
Φ_{max}	Height of DLVO energy barrier [M L^2 t^{-2}]
Φ_{sec}	Depth of DLVO secondary minimum [M L^2 t^{-2}]
ψ_ζ	Zeta potential [M L^2 t^{-3} I^{-1}]
ψ_0	Surface potential [M L^2 t^{-3} I^{-1}]

Latyn symbols

A	Absorbance
A_{rip}	Ripening multiplier
a_c	Radius of the collector [L]
a_{is}	Radius of the inner sphere for hollow particles [L]
a_p	Radius of the particle [L]
B_{rip}	Ripening exponent
C	Particles concentration in the liquid phase [M L^{-3}]
C_0	Particles initial concentration in the liquid phase [M L^{-3}]
CDC	Critical deposition electrolyte concentration [M L^{-3}]
CRC	Critical release electrolyte concentration [M L^{-3}]
c_0	Solute initial concentration in the liquid phase [M L^{-3}]

c_s	Solute concentration in the liquid phase [M L^{-3}]
D_∞	Particle Diffusion coefficient in an infinite medium, $\frac{k_B T}{6\pi\mu a_p}$ [L^2 t^{-1}] [1]
D_x	Solute Dispersion coefficient in the x direction [L^2 t^{-1}]
d_c	Diameter of the collector [L]
d_p	Diameter of the particle [L]
e	Neper number
$f_{a,i}$	Attachment function for i-th site
$f_{d,i}$	Detachment function for i-th site
g	Gravity constant [L t^{-2}]
h	Planck constant [M L^2 t^{-1}]
H	Hamaker constant [M L^2 t^{-2}]
I	Ionic strength [mol L^{-3}]
I_s	Mass flux of particles reaching the collector [M t^{-1}]
k	Inverse Debye-Huckel length [L^{-1}]
$k_{a,i}$	Attachment rate for i-th site [t^{-1}]
$k_{a\infty}$	Asymptotic attachment rate [t^{-1}]
$k_{a,CFT}$	Classical filtration theory filter coefficient [t^{-1}]
k_B	Boltzmann constant [M L^2 t^{-2} T^{-1}]
$k_{d,i}$	Detachment rate for i-th site [t^{-1}]
k_{d0}	Zero detachment rate [t^{-1}]
l	Flow-cell pathlength [L]
M_{in}	Injected particle mass [M]
M_{out}	Recovered particle mass [M]
n	Porous medium porosity
n_a	Avogadro Number [mol^{-1}]
n_e	Porous medium effective porosity
q	Electron charge [I t]
r	Separation distance between surfaces [L]
S_i	Particle concentration in solid phase of i-th site [M M^{-1}]
S_{max}	Maximum particle concentration in solid phase for blocking [M M^{-1}]
T	Absolute temperature [T]
U_e	Electrophoretic mobility [I t^2 M^{-1}]
V_{EDL}	Electrostatic double layer potential [M L^2 t^{-2}]
V_{in}	Injected volume of particle-containing water [L^3]
V_{out}	Recovered volume of particle-containing water [L^3]
V_{TOT}	Total energy potential [M L^2 t^{-2}]
V_{vdW}	Van der Waals energy potential [M L^2 t^{-2}]
v_d	Darcy velocity [L t^{-1}]
v_p	Pore-water velocity [L t^{-1}]
v_{stokes}	Stokes' settling velocity [L t^{-1}]
z	Ion valence

Dimensionless Numbers:

γ	$(1-n)^{1/3}$	Porosity-dependent parameter
Γ_i	$tanh\left[\frac{zq\psi_0}{4k_BT}\right]$	Dimensionless surface potential
A_s	$\frac{2(1-\gamma^5)}{2-3\gamma+3\gamma^5-2\gamma^6}$	Porosity-dependent parameter
N_A	$\frac{H_{132}}{12\pi\mu{a_p}^2 v_p}$	Attraction Number
N_G	$\frac{2{a_p}^2 g\left(\rho_p-\rho_f\right)}{9\mu v_p}$	Gravity Number
N_{Gi}	$\frac{1}{(N_G+1)}$	Gravitational Number
N_{LO}	$\frac{H_{132}}{9\pi\mu{a_p}^2 v_p}$	London-Van der Waals Number
N_{Pe}	$\frac{v_p\, d_c}{D_\infty}$	Peclet Number
N_R	$\frac{a_p}{a_c}$	Aspect Ratio
N_{vdw}	$\frac{H_{132}}{k_BT}$	Van der Waals Number

Acronyms / Abbreviations:

BTC	*Breakthrough Curve*
CFT	*Classical Filtration Theory*
DLS	*Dynamic Light Scattering*
DLVO	*Derjaguin-Landau-Verwey-Overbeek*
ENM	*Engineered Nanomaterial*
IEP	*Isoelectric Point*
MFT	*Modified Filtration Theory*
MNMs	*Micro- and Nanoparticle transport, filtration and clogging Model- suite*
NP	*Nanoparticle*
PV	*Pore Volume*
SEM	*Scanning Electron Microscopy*
TEM	*Transmission Electron Microscopy*

Abstract

In recent years, SiO_2 nanoparticles (NPs) have been extensively investigated for their potential in a wide range of environmental applications, including contaminant adsorption, environmental catalysis or as carriers for encapsulated pesticides. In this study, a combination of experimental methods, including transmission electron microscopy (TEM), scanning electron microscopy (SEM), dynamic light scattering (DLS) and disc centrifuge was used to characterize two sets of hollow and solid silica NPs. NPs transport in sand-packed columns was then studied at various electrolyte concentrations to assess their mobility in typical geochemical conditions. Due to the similarities in their physical properties, solid SiO_2 NPs were used as templates for mesoporous silica particles, that represent the real competitor to hollow spheres for applications as carriers or adsorbents.

Classical theoretical foundations of colloids science, namely Derjaguin-Landau-Verwey-Overbeek (DLVO) theory, single collector contact efficiency and macro-scale transport equations were used for the interpretation of experimental data.

Analysis of breakthrough curves (BTC) revealed high mobility features for both sets of particles, that were consistently able to reach C/C_0 values higher than 0.6. NPs retention within the porous medium increased with increasing ionic strength: in the same chemistry conditions, solid particles showed higher mobility than hollow NPs. These results are in good accordance with single collector efficiency calculations and DLVO interaction energies.

Modelling based on classical filtration theory's (CFT) clean bed hypothesis was not able to approximate experimental BTCs for both hollow and solid particles. Reversible particle-solid phase interactions were found to be better suited to model experimental BTCs and estimated kinetic rates were consistent with data found in literature.

In conclusion, the density difference was proven to be of minimal influence on macro-scale transport, and higher retention levels showed by hollow particles were imputable to surface properties. There is strong evidence that both sets of SiO_2 NPs could behave as vectors for adsorbed contaminants but conclusive evaluations in this regard should be based on transport tests performed on loaded particles.

1. State of knowledge

In this chapter, clarifications on the terminology utilized throughout this work are presented alongside a brief description of nanomaterials features.

Then, some considerations will be introduced on the economic and regulatory landscape in which nanomaterials are being developed and, finally, the environmental relevance of SiO_2 NPs will be assessed discussing the need of a thorough understanding of their behaviour with particular regard for groundwater environment.

1.1 What is nano?

On a scientific level, much debate still exists regarding the definition associated with nanoscience and nanotechnology: in October 2011, with the document *Reccomandations regarding the definition of nanomaterial* [2] published on the official journal of the European union, the European commission proposed to define a nanomaterial as:

"[…] a natural, incidental or manufactured material containing particles, in an unbound state or as an aggregate or as an agglomerate and where, for 50% or more of the particles in the number size distribution, one or more external dimensions is in the size range 1nm-100nm".

Similar definitions have been adopted by other international institutions like the American Society for Testing Materials, the British Standards Institutions and the Scientific Committee on Emerging and Newly-Identified Health Risks [3].

Since even larger particles can exhibit similar properties, the arbitrariness of the 100 nm-threshold has raised issues in the scientific community. In particular, the question has arisen as to whether particular types of nanostructures, designed as carriers for medical, cosmetic, food or agricultural applications, should be considered as nanomaterials. Such nanocarriers, indeed, generally have outer diameters exceeding 100nm even if internal functional properties may be smaller [4,5].

The EU Joint Research Centre report *Considerations on a definition of nanomaterial for Regulatory purposes* [6] suggests that the definition of nanomaterial should be broadly applicable in Union legislation and in line with other approaches worldwide, but recognizes the lack of scientific evidence supporting the choice of the 100 nm upper limit. The European commission therefore has suggested the member states, the union agencies and economic operators to intend the abovementioned definition mainly for regulatory purposes.

Within this broad group of materials, nanoparticles (NPs) have been defined as materials with at least two dimensions between 1nm and 100 nm [3].

In this work, the behaviour of SiO_2 spheres with dimensions ranging from 170nm to few micrometres has been assessed. Despite the EU definition of 'nanomaterial', they will be regularly referred to as nanoparticles.

Moreover, the International Union of Pure and Applied Chemistry (IUPAC) defines a colloid as a state of subdivision in which *"[…] molecules or polymolecular particles dispersed* in a medium have at least in one direction a dimension roughly between 1nm and 1μm" [7]. This definition includes a wide range of different phases dispersed in continuous media, namely liquid and solid aerosols, foams, emulsions etc.

Nanoparticles suspensions represent full-fledged examples of colloidal dispersions, and in the frame of this work the two definitions will be used indistinctly.

1.2 Engineered nanoparticles: market and regulations

"From bacteria that sense the earth's magnetic field using 'nanomagnets,' to the facilitated transport of radionuclides in groundwater, nanoparticles are central to many natural processes. The behaviour of these naturally occurring materials results from their physical size, tunable properties and large and accessible inorganic surfaces". The same features can be optimized in engineered nanomaterials (ENMs) to address specific technologic needs[8].

Nanomaterials display different physico-chemical characteristic with respect to materials of the same composition but of a coarser sizes [6]. Many of these properties (e.g. greater adsorption efficiency, enhanced electrical conductivity, thermal and mechanical stability) are the results of more favourable surface per unit mass ratios occurring at the nanoscale [8,9].From purely geometrical considerations, 1 g of silica nanospheres with a diameter of 10nm exhibits the same surface area of a single sphere by the weight of more than 26 tons.

A scale of reference is shown in *Figure 1.1*.

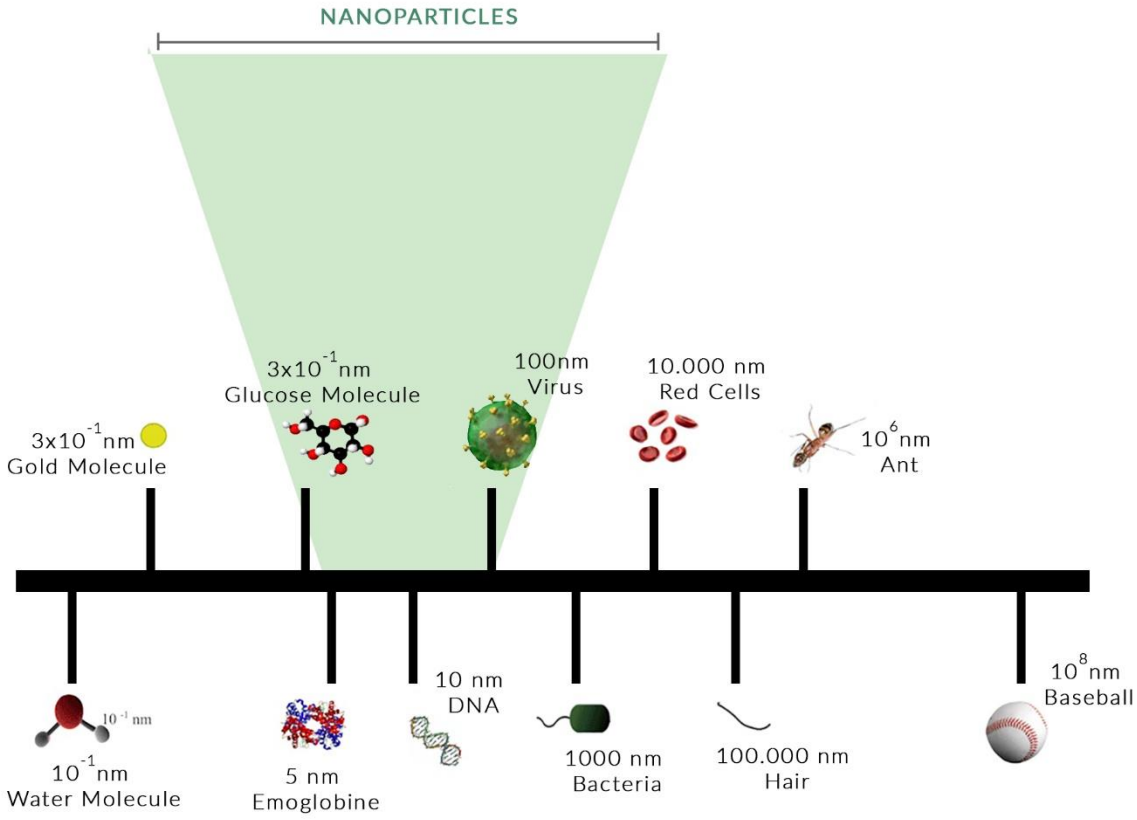

Figure 1.1: Reference scale for size of nanomaterials

Since the late Eighties, nanotechnologies have been increasingly incorporated into commercial products but a conclusive assessment of nanomaterials' market size is still lacking [10]. Much effort has been made by private and public institutions to document the penetration level of nano-enabled products into the commercial marketplace, but inconsistencies between different databases has so far made it difficult to gather reliable and up-to-dated information [11].

In 2005, the Project on Emerging Nanotechnology created the Nanotechnology Consumer Product Inventory (CPI) that it's since become one of the most popular resources of information regarding the market of nanotechnologies. Data gathered from CPI reports from 2007 to 2014 (*Figure 1.2*) show significant increase in the commercialization of nano-enabled products [10], especially among cosmetics and in the personal care field.

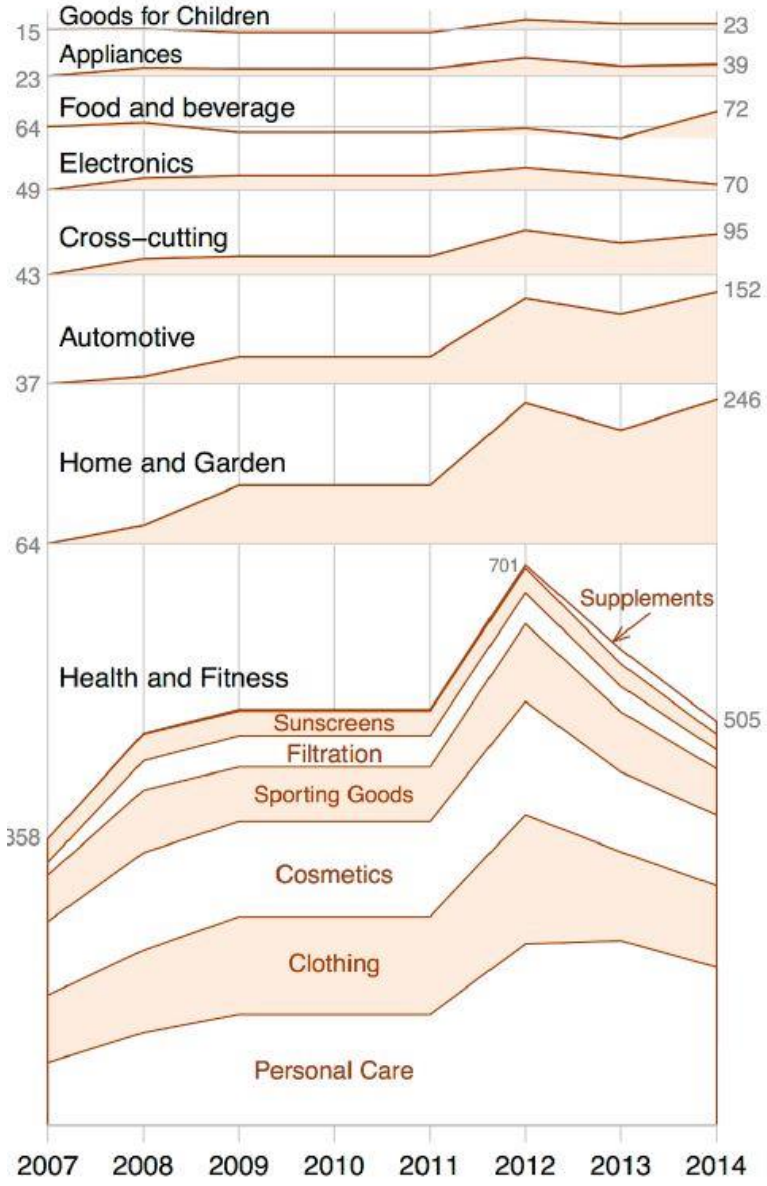

Figure 1.2 : Number of commercial products containing nanomaterials listed in CPI [10]

The fast rate at which products containing nanomaterials are entering the market is not expected to decrease anytime soon: according to different projections, the global market for nanomaterials is forecasted to reach values exceeding USD 11.3 billion before 2020 [11].

In terms of composition, titanium dioxide, silicon dioxide and zinc oxide are the most produced nanomaterials worldwide. Silver nanoparticles, however, have proved to be the most ubiquitous, appearing in almost 25% of the nano-enabled products listed in CPI [10]. In *Figure 1.3,* the claimed composition of nanomaterials listed in CPI is reported.

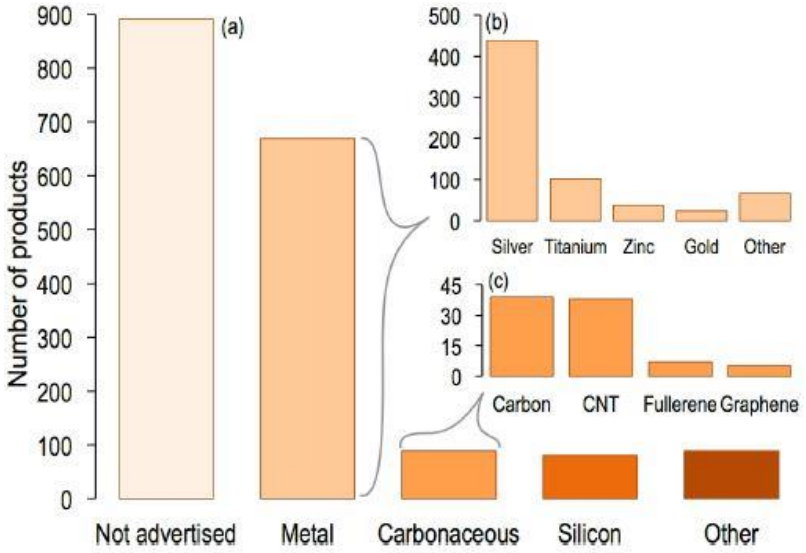

Figure 1.3: Composition of nanomaterials listed in CPI [10]

In this context, as a result of their extremely high sorption capacity and possibility to be functionalized, Si_O_2 NPs (especially mesoporous) have found many applications in biomedical [12], electrochemical [13] and environmental fields [8,9,14]. Among environmental uses, applications like catalysis, separations or gas adsorption are worth mentioning [14]. Use of silica NPs as carriers for pesticides [15–17] or to improve volumetric efficiency for enhanced oil recovery [18] still represent issues of ongoing research.

In the framework of EU regulatory system, nanomaterials are considered key enabling technologies, providing the basis for further development of new products [19]. ENMs are covered by European legislation, either implicitly or explicitly, by a wide number of sector-specific regulations, including REACH regulation (CE n.1907/2006), biocidal products regulation (CE n.528/2012), cosmetic products regulation (CE n.1223/2009), novel food regulation (CE n.2283/2015) and medical devices regulation (COM 542/2014) among others.

Within this complex system of legislation, the rules established by each single law apply only within its subject matter and purpose, and, in spite of the recommendation on the definition mentioned in paragraph 1.1, the definition of nanomaterial itself is not uniquely defined in a regulatory binding way.

The European commission's second regulatory review concluded that nanomaterials should be considered as other chemicals in that some may exhibit relevant toxicity and some may not [19] and that risk assessment of nanotechnologies should then by performed in relation with a specific use on a case-by-case basis.

1.3 Environmental relevance

The rapidly-growing demand of nanotechnology is increasing the production and application of NPs that will inevitably enter the environment and increase the likelihood of human exposure [20,21].

Some of the same properties that make ENMs useful may cause certain nanomaterials to pose hazards to humans and the environment under specific conditions [22]. Size itself is believed to be a potential factor of direct toxicity and pathology, as some particles may be able to enter biological tissues and move through cell membranes or across the blood-brain barrier [22,23].

In addition to their potential role as direct toxic agents, particles may act as secondary sources of contamination transporting adsorbed contaminants [4,20], as schematized in *Figure 1.4*. Many groundwater environments actually present favourable conditions for colloid-facilitated transport of other contaminants [24].

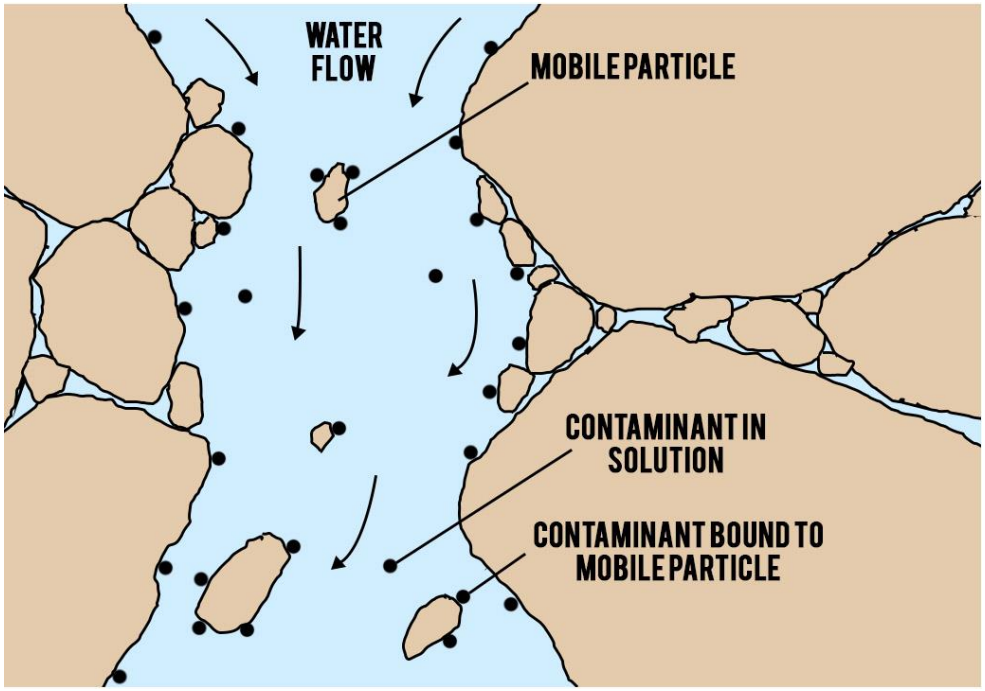

Figure 1.4: Representation of NPs potential role as contaminants carriers

As a result of some of the characteristics mentioned in previous paragraphs, silica NPs have the potential to pose a threat to human health both directly [25] and indirectly. Their potential application as encapsulating shells for pesticides and fertilizers, in particular, may be critical in terms of environmental impacts as it would represent the only intentional diffuse source of ENMs in the environment [4].

2. Fate and transport of colloidal particles in groundwater

Groundwater environments are complex systems in which physical and physico-chemical mechanisms acting at different scales control colloids' mobility and deposition. Whether released as contaminants, for remediation of contaminated aquifers or for agricultural practices, a deep understanding of particle transport in porous media is required to properly assess the risk for human health associated with nanomaterials.

In this chapter, the pore-scale mechanisms governing particle-particle and particle-collector interactions are presented. Then, the partial differential equations used for macro-scale solutes and particles transport are introduced alongside typical kinetics models of deposition/release.

2.1 Pore-scale interactions

The physico-chemical processes that determine whether a particle is transported or retained onto the solid matrix occur at the scale of the pores. In a saturated porous medium, the collector grains are generally considered to be immobile and particles move suspended in water as per *Figure 2.1*.

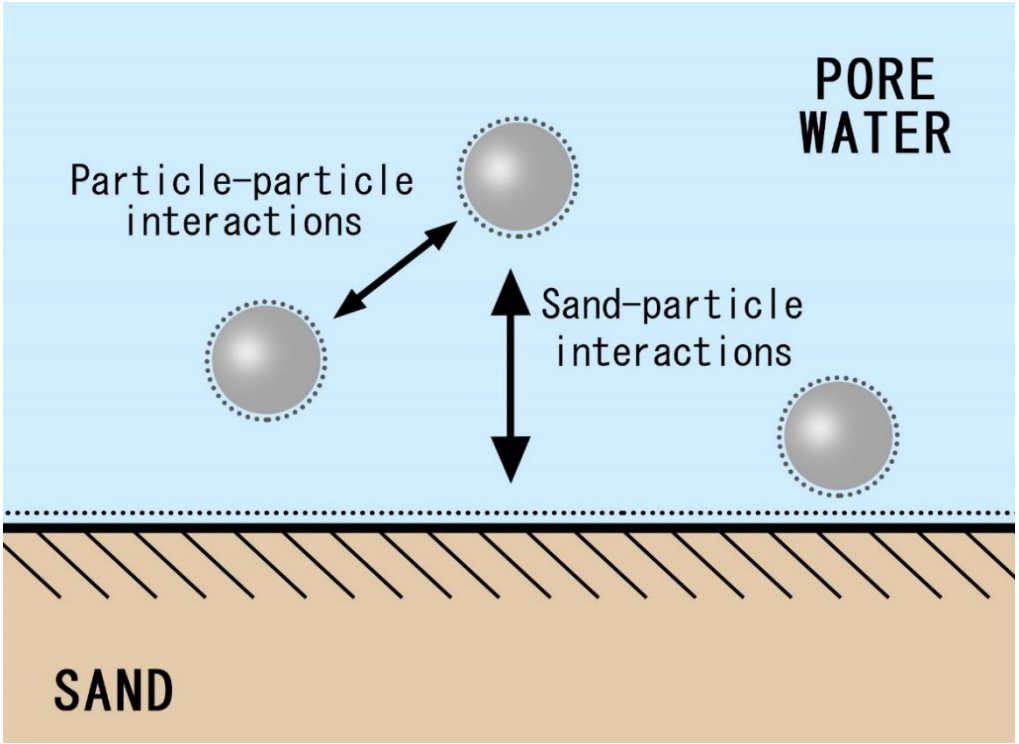

Figure 2.1: Conceptual model of pore-scale interactions

NPs and solid grains' physical properties affecting particle-particle and sand-particle interactions include particle's dimensions and surface charge. Chemical features of the colloidal suspension, namely pH, ionic strength and colloids coating, can also influence NPs behaviour in porous media.

2.1.1 DLVO theory

The Derjaguin-Landau-Verwey-Overbeek (DLVO) theory [26,27] defines the interaction forces between two charged surfaces immersed in an homogeneous medium controlling particles stability and their aggregation behaviour. Classical DLVO takes into account the effects of attracting van der Waals forces and repulsive electrostatic forces, but a number of authors have introduced formulations to include other nano-scale interactions, namely Born, steric and magnetic [28–30]. Since those interactions have proven to be insignificant for non-coated SiO_2 NPs [18,20,31], for the sake of brevity, they will be excluded from this dissertation.

Classical DLVO theory is based on the assumption of additionality of forces, that expresses the total potential energy between two charged surfaces as the sum of van der Waals and electrostatic double layer contributions (2.1).

$$V_{TOT} = V_{vdW} + V_{EDL} \tag{2.1}$$

Van der Waals forces are generated from the interactions between atomic or molecular oscillating or rotating electrical dipoles within the interacting media: Keesom force (between permanent dipoles), Debye force (between one permanent dipole and one induced dipole) and London force (between two permanent dipoles) contribute to the van der Waals force.

Electrostatic repulsive forces arise when two particles approach one another and their electrical double layers interact with each other opposing coagulation [32].

Analytical formulations for particle-particle and particle-collector interactions are derived for systems as per *Figure 2.2*: particles are considered to be homogeneous spheres with small dimensions relative to solid grains that can therefore be modelled as plates.

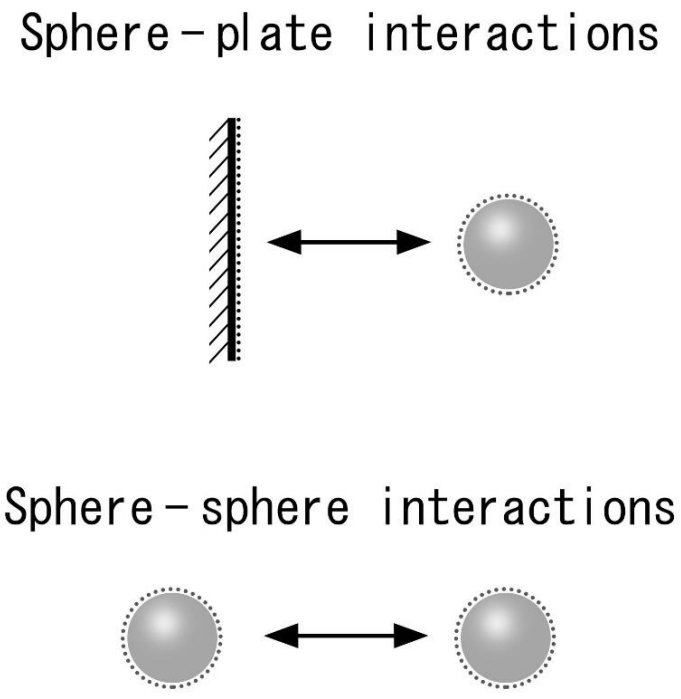

Figure 2.2: Geometrical scheme for particle-particle and sand-particle interactions modeling

Gregory developed analytical solutions for van der Waals interactions in both geometrical conditions [33]. Expressions for sphere-sphere (2.2) and sphere-plate (2.3) interactions are valid for $r \ll a_p$.

$$V_{wdv} = -\frac{H_{131}\, a_p}{12\, r\, (1 + 14\frac{r}{\lambda})} \tag{2.2}$$

$$V_{wdv} = -\frac{H_{132}\, a_p}{6\, r\, (1 + 14\frac{r}{\lambda})} \tag{2.3}$$

where H_{131} [M L^2 T^{-2}] is the global Hamaker constant of the system, a_p [L] is the particle radius, r [L] is the separation distance between the two surfaces and λ [L] is the characteristic wavelength of the interaction, usually assumed equal to 100nm.

The global Hamaker constant represents a conventional way of assessing the magnitude of Van der Waals interaction and is obtained as a combination of the physical properties of the three media composing the system as per *Figure 2.3*.

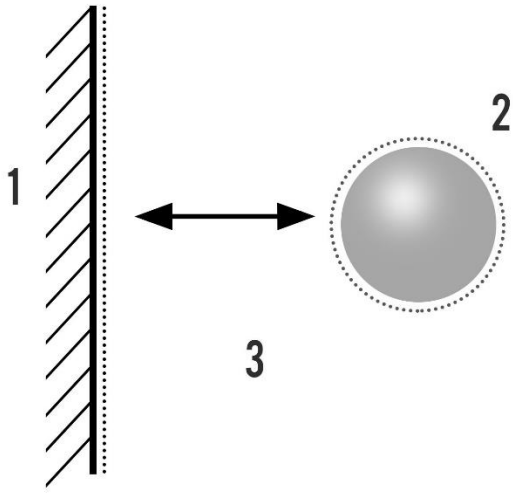

Figure 2.3: Conceptual model for calculation of the global Hamaker constant

Lipkin et al. [34] derived from Lifshitz theory an analytical expression for global Hamaker constant calculation (2.4):

$$H_{132} = \frac{3k_B T}{4}\left(\frac{\varepsilon_{r,1} - \varepsilon_{r,3}}{\varepsilon_{r,1} + \varepsilon_{r,3}}\right)\left(\frac{\varepsilon_{r,2} - \varepsilon_{r,3}}{\varepsilon_{r,2} + \varepsilon_{r,3}}\right) + \frac{3h\nu_e}{8\sqrt{2}}\left[\frac{\left({\delta_1}^2 - {\delta_3}^2\right)\left({\delta_2}^2 - {\delta_3}^2\right)}{\sqrt{\left({\delta_1}^2 + {\delta_3}^2\right)\left({\delta_2}^2 + {\delta_3}^2\right)}\sqrt{\left({\delta_1}^2 + {\delta_3}^2\right) + \left({\delta_2}^2 + {\delta_3}^2\right)}}\right] \tag{2.4}$$

being k_B (1.38×10^{-23} J/K) the Boltzmann constant, T [T] the absolute temperature, $\varepsilon_{r,i}$ the relative dielectric constant of i-th medium, h (6.626×10^{-34} Js) the Planck's constant, ν_e (3×10^{15} s^{-1}) the electronic absorption frequency in the UV region and δ_i the refractive index of i-th medium.

For hollow particles in which interior and exterior fluids are the same, the van der Waals energy profile is usually calculated by subtracting the VdW energies of the inner and outer [35,36] (2.5).

$$V_{vdW} = {V_{vdW}}^{OUT} - {V_{vdW}}^{IN} \tag{2.5}$$

Electrical double layer interactions arise when a charged particle is suspended in a fluid domain [32]. Electrostatic effects attract within the inner layer (Stern layer) ions with opposite charge that of the particle's surface; beyond Stern layer, electrostatic interactions decrease and after a Debye length, in correspondence of the shear plane, electrical field is considered to be reduced by a factor of $1/e$ [37]. The Debye length is the distance assumed to work as a threshold between the charged particle and the dispersant medium, and the value of potential is defined as zeta-potential ψ_ζ (*Figure 2.4*).

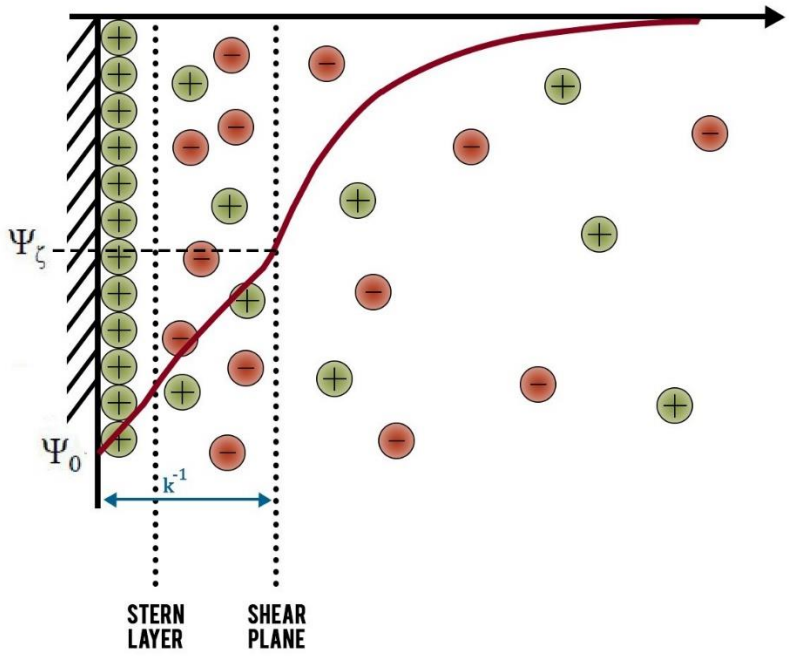

Figure 2.4: Schematic representation of the electrical double layer

Gregory [38] introduced sphere-sphere (2.6) and sphere-plate (2.7) formulations for electrostatic double-layer interactions, based on the linear superposition approximation: these expressions are valid for $ka_p \gg 1$ [21].

$$V_{EDL} = 64\pi\varepsilon_0\varepsilon_r \frac{a_{p,1}\, a_{p,2}}{a_{p,1} + a_{p,2}} \left(\frac{k_B T}{zq}\right)^2 \Gamma_1\Gamma_2 e^{-kr} \tag{2.6}$$

$$V_{EDL} = 64\pi\varepsilon_0\varepsilon_r a_p \left(\frac{k_B T}{zq}\right)^2 \Gamma_1\Gamma_2\, e^{-kr} \tag{2.7}$$

being ε_0 [I² t⁴ M⁻¹ L⁻³] the vacuum dielectric constant, $\Gamma_{1,2} = tanh\left[\frac{zq\psi_0}{4k_BT}\right]$ the dimensionless surface potentials, z the ion valence, q [I t] the electron charge and k [L⁻¹] the inverse Debye-length.
The Debye length k^{-1} is calculated as [39]:

$$k^{-1} = \sqrt{\frac{\varepsilon_o\varepsilon_r k_B T}{q^2 n_a 2I}} \tag{2.8}$$

where n_a [mol⁻¹] is the Avogadro number and $I = \sum {z_i}^2 c_i$ [mol L⁻³] is the solution ionic strength.

Double layer interactions are surface forces and the influence of the inner sphere can be neglected for calculations of the electrostatic potential of hollow NPs [36].

An example of typical DLVO energy profile is reported in *Figure 2.5*. Typical features of interactions energy profiles are deep primary minima (wells) at small separation distances, maximum energy barriers and shallow secondary wells at larger separation distances [39]. In conditions commonly found in colloids' science, DLVO interactions disappear within few tens of nanometres.

In absence of close-range repulsive (e.g. Born) interactions, when a particle is able to overcome the energy barrier it is considered to be irreversibly attached either to a different particle or to the collector as the magnitude of forces in the primary well prevents further re-mobilizations. If a NP is not able to overcome the energy barrier, it can be retained in a secondary minimum: this condition is considered to be reversible as modifications in solution chemistry (e.g. pH, ionic strength) can lead to detachment.

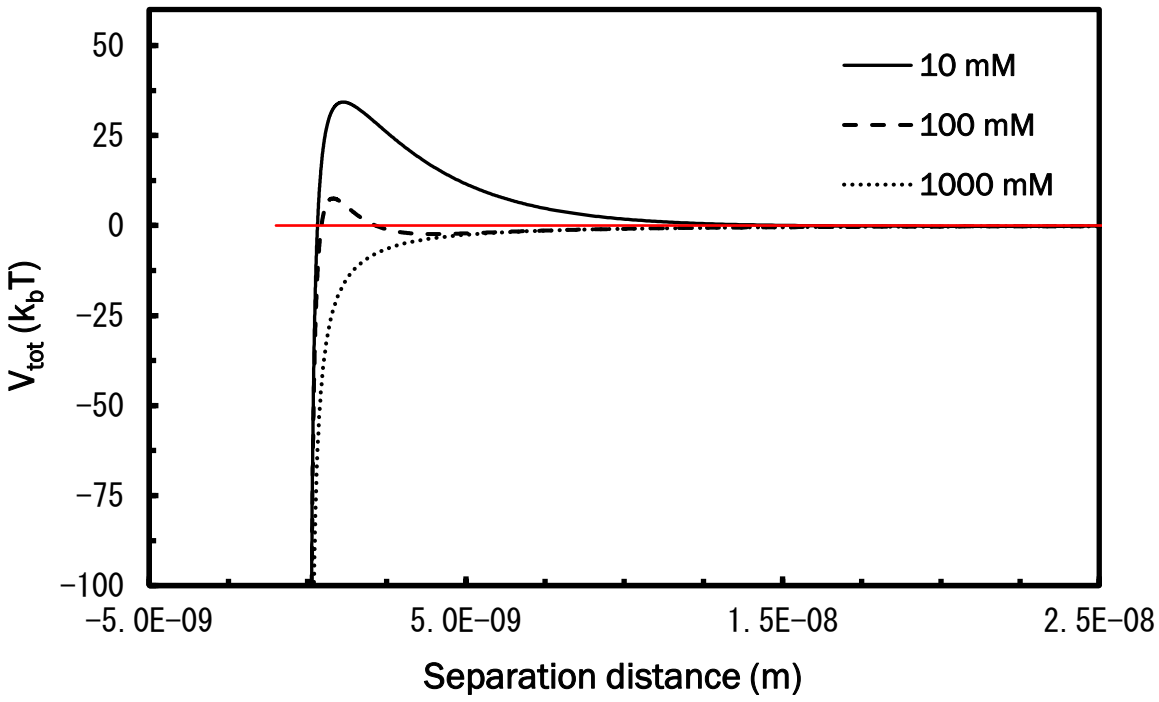

Figure 2.5: Typical DLVO energy profiles

Figure 2.5 shows the effects of ionic strength on DLVO interaction energy profiles. Increasing values of ionic strength results in a compression of the electrical double layer, thus leading to favourable attachment/aggregation conditions. Curves at 10 mM, 100 mM and 1000 mM are respectively representative of (i) stable NPs suspensions, unlikely to aggregate or be retained by the porous medium, (ii) partially stable NPs suspensions, likely to be subject to reversible aggregation or attachment and (iii) unstable NPs suspensions in which the favourable aggregation regime is likely to produce large agglomerates and strongly limit particles mobility in porous media.

2.1.2 Single collector contact efficiency

Classical filtration theory (CFT) describes the deposition of suspended particles onto porous media grains as a two-step process [40]: (i) the transport of particles to the collector surface, quantified by the single collector contact efficiency η_0 and (ii) the physico-chemical deposition to the collector surface, as described by DLVO theory, quantified by the attachment efficiency α.

For a single spherical grain of filter medium unaffected by its neighbours and fixed in an infinite fluid domain, single collector contact efficiency is calculated as the ratio of the rate at which particle strike the collector to the convective transport of particles towards the projected area of the collector [40,41]:

$$\eta_0 = \frac{I_s}{v_p C_0 (\pi {a_c}^2)} \tag{2.9}$$

being I_s [M t^{-1}] the mass flux of particles colliding with the collector, v_p [L t^{-1}] the pore-water velocity, C_0 [M L^{-3}] the concentration of suspended particles in the incoming flow and a_c [L] the collector radius.

As suspended particles are transported in proximity of the porous media grains by advection in the bulk fluid, three mechanisms can be responsible for actual particle-collector contact as shown in *Figure 2.6*:

- ***Sedimentation by gravity***: if the density of the suspended particle is greater than that of the water, the particle follows a different trajectory due to the influence of gravitational force field.
- ***Interception***: a suspended particle following a streamline of the flow may come in contact with the collector by virtue of its own size.
- ***Brownian diffusion***: particles can divert from fluid streamlines for effect of Brownian thermal motion [1], thus coming in contact with the collector.

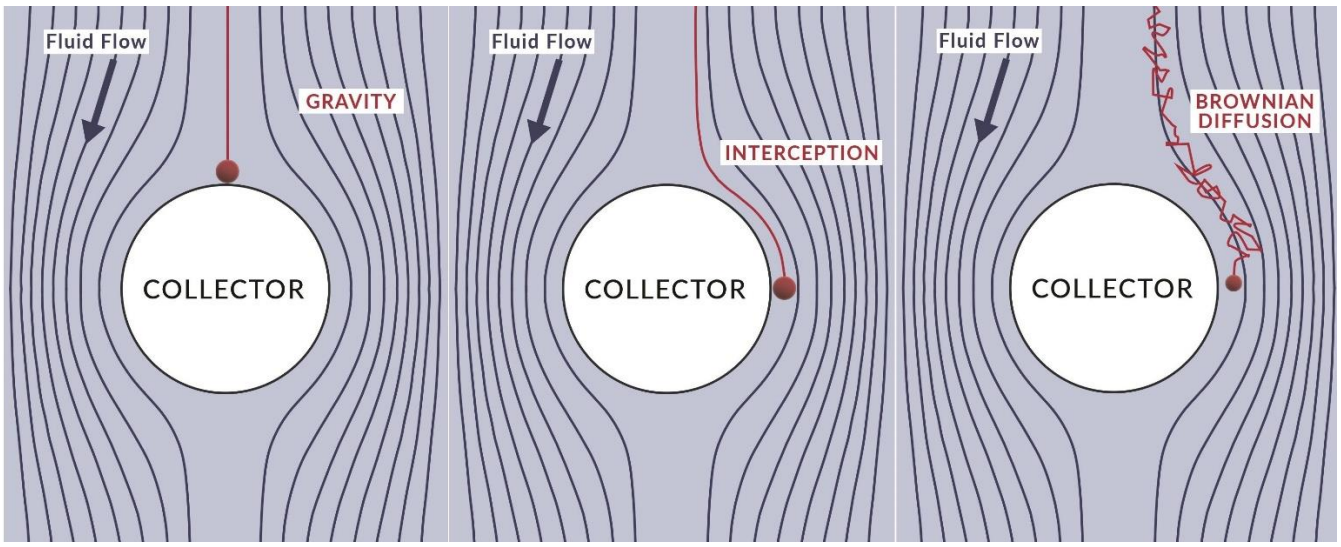

Figure 2.6: CFT collision mechanisms

Under the assumption of additionality of effects, single collector contact efficiency can be calculated as the sum of contact efficiencies of the single mechanisms [40,42,43].

$$\eta_0 = \eta_D + \eta_G + \eta_I \tag{2.10}$$

Being η_D is the single collector efficiency due to brownian diffusion, η_G is the single collector efficiency due to gravity and η_I is the single collector efficiency due to interception.

The influence of the three mechanisms on particle filtration depends on the characteristics of particles (e.g. size, Hamaker constant and density), of the porous medium (e.g. collector's size, porosity) and of the fluid flow (e.g. temperature, pore-water velocity). Interception and gravity effects dominate for bigger particles, while Brownian diffusion prevails at small particles' size.

A number of empirical formulations have been developed for the prediction of single collector contact efficiency accounting for CFT's contact mechanisms and further effects (e.g. van der Waals forces, fluid drag, hydrodynamic retardation). All formulations, as reported in *Table 2.2*, are expressed as a function of the following dimensionless groups (see *Nomenclature* for reference):

$$\eta_0 = \eta_0(\gamma, A_s, N_A, N_G, N_{Gi}, N_{LO}, N_{Pe}, N_R,\ N_{vdw}) \tag{2.11}$$

Equations from (2.13) to (2.18) have been developed from trajectory simulations either based on Happel's sphere-in-cell [44] or Ma's "hemisphere-in-cell" [45] fluid models and are valid for the range of values reported in *Table 2.1*.

Table 2.1: Values of parameters used in trajectory simulations for prediction of single collector contact efficiency

Formulation	Particle diameter (μm)	Collector diameter (mm)	Hamaker constant (J)	Pore-water velocity (m/s)	Particle density (g/cm³)
Yao et al. (1971)	0.01 - 100	0.5, 1	n.a.	1.4×10^{-3}, 2.7×10^{-3}	1, 1.05, 2.6
Rajagopalan-Tien (1976)	n. a.	n. a.	n. a.	n. a.	n. a.
Tufenkji-Elimelech (2004)	0.01 - 10	0.05 – 0.5	3×10^{-21} - 4×10^{-20}	7×10^{-6} - 2×10^{-3}	1 – 1.8
Ma et al.(2009)	n. a.	0.51	3.84×10^{-21}	1.7×10^{-5}	1.055
Nelson-Ginn (2011)	0.01 - 10	0.01 – 1.2	3×10^{-21} - 4×10^{-20}	1×10^{-7} - 2×10^{-3}	1 – 1.8
Ma et al. (2013)	0.01 - 10	0.51	3.84×10^{-21}	4.6×10^{-7} - 4.6×10^{-5}	1.055, 4

The second step of particle deposition is governed by DLVO particle-collector interactions: the attachment efficiency α quantifies the number of collided particles that remain deposited on the collector surface with respect to the total number of collisions defined by η_0.

To simultaneously account for both processes, the single collector removal efficiency can be calculated as [21]:

$$\eta = \alpha\eta_0 \tag{2.12}$$

Table 2.2: Formulations for prediction of single collector contact efficiency

Yao et al. (1971) [40]	$\eta_0 = 4.04 {N_{Pe}}^{-\frac{2}{3}} + N_G + \frac{3}{2} {N_R}^2$	(2.13)
Rajagopalan-Tien (1976) [46]	$\eta_0 = 4.04 {N_{Pe}}^{-\frac{2}{3}} {A_S}^{0.333} + A_S {N_R}^{1.875} {N_{LO}}^{0.125} + 0.00338 A_S {N_G}^{1.2} {N_R}^{-0.4}$	(2.14)
Tufenkji-Elimelech (2004) [41]	$\eta_0 = 2.4 {A_S}^{0.333} {N_{Pe}}^{-0.715} {N_R}^{-0.081} {N_{vdw}}^{0.052} + 0.55 A_S {N_R}^{1.675} {N_A}^{-0.125} + 0.22 {N_G}^{1.11} {N_R}^{-0.24} {N_{vdw}}^{0.053}$	(2.15)
Ma et al. (2009) [45]	$\eta_0 = 2.3 {A_S}^{0.333} {N_A}^{0.052} {N_R}^{-0.08} {N_{Pe}}^{-0.65} + 0.55 A_S {N_R}^{1.8} {N_A}^{0.15} + 0.2 {N_G}^{1.11} {N_R}^{-0.10} {N_{Pe}}^{0.053} {N_A}^{0.053}$	(2.16)
Nelson-Ginn (2011) [47]	$\eta_0 = 2.4 {A_s}^{0.333} \left(\frac{N_{Pe}}{N_{pe}+16}\right)^{0.75} {N_{Pe}}^{-0.68} {N_{Lo}}^{0.015} {N_{Gi}}^{0.8} + A_s {N_{Lo}}^{0.125} {N_R}^{1.875} + 0.7 \left(\frac{N_{Gi}}{N_{Gi}+0.9}\right) N_G {N_R}^{-0.05}$	(2.17)
Ma et al. (2013) [48]	$\eta_0 = \frac{8 + 4(1-\gamma) {A_S}^{0.333} {N_{pe}}^{0.333}}{8 + 4(1-\gamma) {N_{pe}}^{0.97}} {N_{LO}}^{0.015} {N_{Gi}}^{0.8} {N_R}^{0.028} + A_S {N_R}^{1.875} {N_{LO}}^{0.125} + 0.7 {N_R}^{-0.05} N_G \left(\frac{N_{Gi}}{N_{Gi}+0.9}\right)$	(2.18)

2.2 Macro-scale modelling

Quantitative analysis of colloid mobility is of pivotal importance in optimizing the introduction of ENMs in the environment and predicting their fate after release.

In paragraphs 2.2.1 and 2.2.2, equations governing solutes and colloids transport are presented: analysis of experimental breakthrough curves (BTCs) with these models enables the estimation of, respectively, the hydrodynamic parameters of the porous medium and kinetics coefficient of particles deposition.

2.2.1 Solute transport

Since suspended particles are transported along the liquid phase (see *Figure 1.4*), a thorough understanding of dissolved species' mass transport is required to correctly assess colloids' fate in groundwater environments.

The simultaneous action of hydrological (e.g. advection, hydrodynamic dispersion), physico-chemical (e.g. sorption) and biological (e.g. biodegradation) mechanisms is responsible for dissolved species' transport in granular media [49]: for the sake of brevity, only mechanisms relevant for colloids transport, namely advection and hydrodynamic dispersion, will be assessed in this study.

Advection is the process by which a solute is transported by the liquid phase along the flow direction with velocity equal to pore-water velocity v_p. Pore-water velocity is usually obtained as:

$$v_p = \frac{v_d}{n_e} \tag{2.19}$$

being v_d [L t^{-1}] the Darcy velocity and n_e effective porosity of the granular medium n_e. In column transport tests, the Darcy velocity is calculated as the ratio between the injected water flow rate and the column's cross section.

Hydrodynamic dispersion is the phenomenon due to combined action of molecular diffusion (related to thermal movement of solute molecules) and mechanical dispersion (consequence of porous medium's heterogeneities): for pore-water velocities typically found in groundwater systems, molecular diffusion's contribution is negligible and hydrodynamic dispersion coincides with mechanical dispersion [49].
Effects of hydrodynamic dispersion include a non-uniform distribution of velocities along the flow direction and an added mass flux in perpendicular directions. In particular, dispersion is caused by a non-uniform distribution of velocities within a pore-throat [Figure 2.7 (a)], different water velocities within distinct pores [*Figure 2.7* (b)] and the growth of transversal velocities components related to the intricacies of pathways [*Figure 2.7* (c)] [50].

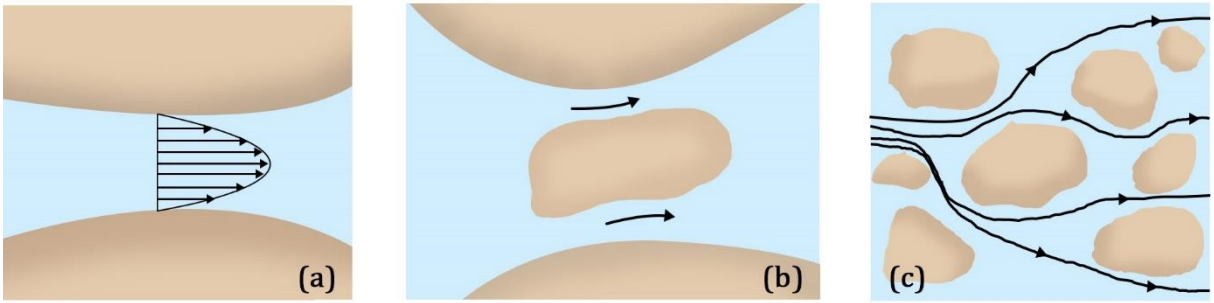

Figure 2.7: Causes of hydrodynamic dispersion

The magnitude of dispersion effects is expressed by dispersion coefficient D [L^2 t^{-1}]. Due to their low diameter-to-length ratio, sand-packed columns are usually modelled as 1D systems [51,52] in which dispersion coefficient along the flow direction is expressed as [49]:

$$D_x = \alpha_x \, v_p \tag{2.20}$$

where α_x [L] is the granular medium's dispersivity in the flow direction.

Dispersion phenomena are analytically modelled with a Fickian approach [50].

Assuming the x-axis coincident with flow direction, the partial differential equation for transport of a non-reactive solute in 1D geometry can be written as:

$$\frac{\partial c_s}{\partial t} = D_x \frac{\partial^2 c_s}{\partial x^2} - v_p \frac{\partial c_s}{\partial x} \tag{2.21}$$

where c_s [M L^{-3}] is the solute concentration in the liquid phase.

Equation (2.21) is valid under the assumptions of (i) homogeneous, saturated and isotropic medium, (ii) conditions of validity of Darcy's law and (iii) density and viscosity of the fluid constant and independent from solute concentration [49].

Transport tests are carried out injecting a constant solute concentration at the inlet of the sand-packed column. Initial and boundary conditions describing constant input for a semi-infinite geometry can be written as:

$$\begin{cases} c_s(x, t = 0) = 0 & for\ x \geq 0 \\ c_s(x = 0, t) = c_0 & for\ t \geq 0 \\ c_s(x = \infty, t) = 0 & for\ t \geq 0 \end{cases} \tag{2.22}$$

where c_0 [[M L^{-3}] is the constant concentration of the injected solute in the liquid phase.

Ogata and Banks [53] developed an analytical solution to equation (2.21) for the set of initial and boundary conditions (2.22):

$$c_s(x, t) = \frac{c_0}{2}\left\{erfc\left[\frac{x - v_p t}{2\sqrt{D_x t}}\right] + exp\left(\frac{v_p\, x}{D_x}\right) erfc\left[\frac{x - v_p t}{2\sqrt{D_x t}}\right]\right\} \tag{2.23}$$

Where $erfc\left[\frac{x-v_p t}{2\sqrt{D_x t}}\right] = 1 - erf\left[\frac{x-v_p t}{2\sqrt{D_x t}}\right]$ is the complementary error function.

$$erf\left[\frac{x - v_p t}{2\sqrt{D_x t}}\right] = \frac{2}{\sqrt{\pi}} \int_0^{\left[\frac{x-v_p t}{2\sqrt{D_x t}}\right]} e^{-y^2} dy$$

Analysis of tracer tests with equation (2.23) enables the estimation of the hydrodynamic parameters of the porous medium, namely n_e and α_x.

2.2.2 Colloids transport

In modelling colloids transport in saturated porous media, the liquid phase advective-dispersive behaviour has to be coupled with a kinetic equation describing particles' interaction with the solid phase [18,54]. To account for the possibility of multisite interactions, the model can be written as:

$$\begin{cases} \dfrac{\partial C}{\partial t} = D_x \dfrac{\partial^2 C}{\partial x^2} - v_p \dfrac{\partial C}{\partial x} - \dfrac{\rho_b}{n} \sum_i \dfrac{\partial S_i}{\partial t} \\ \rho_b \dfrac{\partial S_i}{\partial t} = n k_{a,i} f_{a,i} C - \rho_b k_{d,i} f_{d,i} S_i \end{cases} \tag{2.24}$$

where C [M L^{-3}] is the NPs concentration in the liquid phase, ρ_b [M L^{-3}] the bulk density of the porous medium, n the porous medium porosity, S_i [M M^{-1}] the particle concentration in the solid phase for i-th site, $k_{a,i}$ [t^{-1}] the attachment rate for i-th site, $f_{a,i}$ the attachment function for i-th site, $k_{d,i}$ [t^{-1}] the detachment rate for i-th site and $f_{d,i}$ the detachment function for i-th site.

The second equation represents a generic expression for particles' interaction with the solid phase: by modifying attachment and detachment functions $f_{a,i}$ and $f_{d,i}$, equations (2.24) can be tuned to model different deposition/release kinetics.

Typical particles-porous medium interactions, shown in *Figure 2.8*, are described as follows:

- ***Mechanical filtration*** *[Figure 2.8(a)]* occurs when particles large compared to pores' size obstruct a possible streamline pathway.
- ***Clean bed filtration*** *[Figure 2.8(b)]* describes the early stage of colloid deposition when interactions between attached and suspended particles approaching the san grain are supposed to be negligible.

  CFT's filtration equations are derived assuming the sand-packed bed as an assemblage of isolated spheres [40,55], an hypothesis that reflects the condition of clean bed where particle-particle interactions are neglected.

  CFT's model is based on the assumption of an ideal plug flow filter in steady-state conditions following 1st order linear (f_a=1) irreversible (f_d=0) deposition kinetics, thus leading to an exponential decrease of attached particles with increasing distance [52,56]. A formulation for macro-scale attachment rate as a function of single collector removal efficiency is given as:

$$k_{a,CFT} = \frac{3\,(1-n_e)}{2\,d_c} v_p \alpha \eta_0 \tag{2.25}$$

  Where $k_{a,CFT}$ [t^{-1}] is the attachment rate for CFT and d_c [L] is the median collector diameter. Due to its strict underlying assumptions, CFT is not suited to model late stages of deposition, when particle-particle interactions have significant influence on colloids mobility.
- ***Linear reversible attachment*** can be observed when particle-particle and particle-collector interaction energies are similar [52] and present an energy barrier and a secondary minimum. In this condition, particles are either retained in or released from the secondary minimum and the interactions is modelled by a linear kinetic in which deposited particles have no influence on incoming colloids' transport (f_a=1). Attachment of NPs to the granular medium's grains can be reversible (f_d=1).

- ***Blocking*** *[Figure 2.8(c)]* phenomena occur when strongly repulsive particle-particle interactions (see paragraph 2.1.1) prevent incoming particles' attachment due to the presence of deposited particles. This mechanism is modelled as a saturation process ($f_a = 1 - \frac{S}{S_{max}}$), but colloid deposition can be reversible (f_d=1). S_{max} [M M^{-1}] represents the particle concentration in the solid phase preventing further net deposition. Particles showing strongly positive surface charge are likely to be subjected to blocking phenomena.
- ***Ripening*** *[Figure 2.8(d)]* effects take place when attractive sphere-sphere interactions promote deposition in later stages as attached particles tend to attract incoming particles. As for blocking, ripening phenomena can be explained by DLVO theory. Ripening is modelled by a non-linear attachment kinetics ($f_a = 1 + A_{rip}\, S^{B_{rip}}$), with k_a progressively increasing ($A_{rip} > 0, B_{rip} > 0$) till clogging of the porous medium[52,54]. Particles exhibiting strong magnetic interaction are likely to be subjected to ripening.
- ***Straining*** *[Figure 2.8(e)]* is the trapping of colloidal particles in down-gradient pore throats that are too small to allow particle passage: Bradford et al. [57] suggested that straining is likely to occur for $\frac{a_p}{a_c}$ ratios larger than 1.7×10^{-3}. "The number of dead-end pores is hypothesized to decrease with increasing distance because size exclusion and/or limited transverse dispersivity tend to keep colloids within larger networks bypassing smaller pores", thus making straining more relevant near the column inlet [58]. This interaction is described by a non-linear ($f_a = \left[\frac{d_{50}+x}{d_{50}}\right]^{-\beta_{str}}$) kinetic model.

Models that are able to describe abovementioned interactions are sometimes defined as Modified Filtration Theory (MFT) [18].

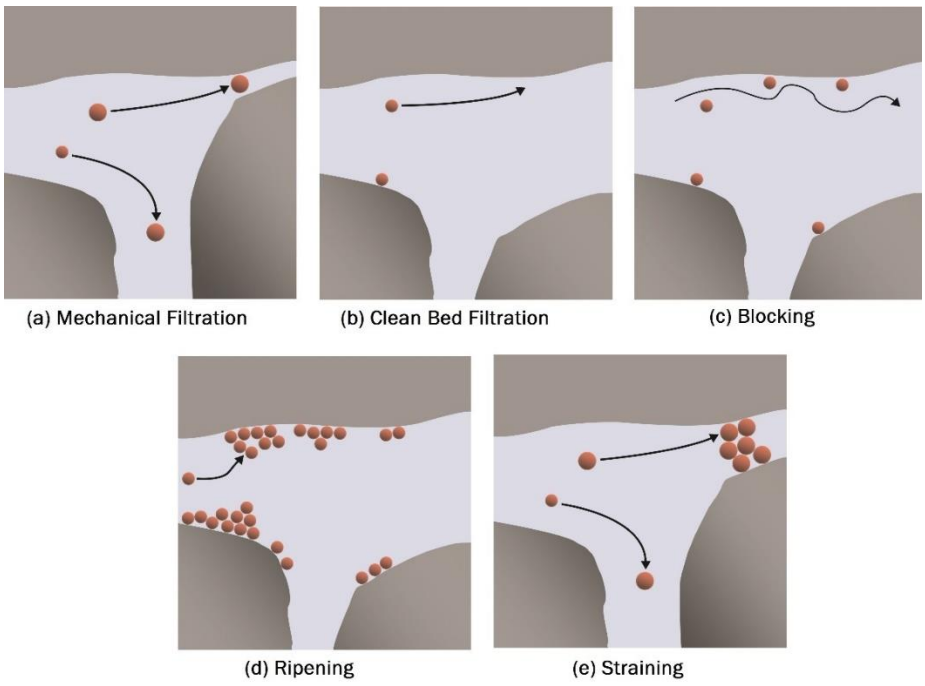

Figure 2.8: Typical interactions between nanoparticles and porous medium's grains

In many cases, NPs retention to solid grains is the consequence of both physical (e.g. mechanical filtration, straining) and physico-chemical (e.g. blocking, ripening) processes: multisite modelling enables to account simultaneously for two or more interactions.

A summary of attachment and detachment functions for typical particles-porous medium interactions is reported in *Table 2.3*.

Table 2.3: Attachment and detachment functions for typical particles-porous medium interactions

Mechanism	f_a	f_d
Mechanical filtration	1	1
Straining	$\left[\frac{d_{50}+x}{d_{50}}\right]^{-\beta_{str}}$	1
Clean Bed Filtration	1	0
Linear	1	1
Blocking	$1-\frac{S}{S_{max}}$	1
Ripening	$1+A_{rip}\,S^{B_{rip}}$	1

As mentioned above, mechanisms regulating particles' transport in granular media are deeply influenced by DLVO interaction energies. Chemical features of the colloidal suspension, namely pH and ionic strength, can affect DLVO energy profiles respectively by modifying surface properties [59–61] or double layer interactions [26,27,32,38].

On a macro-scale transport level, changes in interaction energies result in a modification of attachment and detachment rates and, potentially, of the interaction mechanism between NPs and porous medium. To account for such effects, Tosco et al.[62] developed the following relations correlating macro-scale kinetic rates with ionic strength:

$$k_a = \frac{k_{a\infty}}{1+\left(\frac{CDC}{c_s}\right)^{\beta_a}} \tag{2.26}$$

$$k_d = \frac{k_{d0}}{1+\left(\frac{c_s}{CRC}\right)^{\beta_d}} \tag{2.27}$$

$$S_{max} = \gamma_s\, {c_s}^{\beta_s} \tag{2.28}$$

Where $k_{a\infty}$, CDC, β_a, k_{d0}, CRC, β_d, γ_s, and β_s are empirical coefficients obtained via fitting procedures.

Equation (2.24) suggests that, for ionic strength values higher than the critical deposition concentration CDC, the electrical double layer compression results in favourable (fast) attachment conditions and electrolyte concentration no longer affects the attachment rate k_a: $k_{a\infty}$ therefore represents the asymptotic value of deposition kinetics [51,62].

A symmetrical behaviour is hypothesized for detachment phenomenon [63]: at ionic strength values lower than the critical release concentration CRC, conditions for favorable (fast) detachment are completely developed and detachment rate k_d tends to its asymptotic value k_{d0}.

Due to the linear dependence on a log-log scale shown by experimental data, a power function is used to model variations of maximum concentration in the solid phase with ionic strength.

To couple expressions (2.26), (2.27) and (2.28) to the overall system for colloids transport modelling, an equation describing variation of ionic strength needs to be added [62,64]. Combining advective-dispersive equation for conservative solutes (2.21) to the set of equations (2.24) the multisite model for particles transport in transient ionic strength is obtained as:

$$\begin{cases} \dfrac{\partial c_s}{\partial t} = D_x \dfrac{\partial^2 c_s}{\partial x^2} - v_p \dfrac{\partial c_s}{\partial x} \\ \dfrac{\partial C}{\partial t} = D_x \dfrac{\partial^2 C}{\partial x^2} - v_p \dfrac{\partial C}{\partial x} - \dfrac{\rho_b}{n} \sum_i \dfrac{\partial S_i}{\partial t} \\ \rho_b \dfrac{\partial S_i}{\partial t} = n k_{a,i}(c_s)\, f_{a,i} C - \rho_b k_{d,i}(c_s) f_{d,i} S_i \end{cases} \tag{2.29}$$

Analysis of particles' BTCs with the set of equations (2.29) enables the estimation of kinetic coefficients and critical concentrations governing macro-scale NPs' transport.

2.2.3 Mass Balance

Evaluations on mass balance, alongisde DLVO interaction energies and the shape of BTCs, are an efficient way of assessing whether particles are completely transported or retained by the porous medium, either for physical (e.g. straining, mechanical filtration, trapped in dead-end pores) or physico-chemical (e.g. retained in a primary or secondary minimum) reasons.

Quantitative mass balance analysis can be expressed as:

$$\Delta M = M_{in} - M_{out} \tag{2.30}$$

$$M_{in} = C_0\, V_{in} \tag{2.31}$$

$$M_{out} = \sum \left(\frac{C}{C_0}\right) C_0\, V_{out} \tag{2.32}$$

Where M_{in} [M] is the total injected mass of particles, M_{out} [M] is the mass of particles that have reached the outlet of the column, V_{in} [L³] and V_{out} [L³] are respectively the injected water volume and the volume flowed out of the column. For column transport tests, the hypothesis of $V_{in} = V_{out}$ is assumed.

Mass balance can help predicting whether future changes in geochemical conditions (e.g. reduction of pH, decrease in salt concentration) can lead to remobilization of deposited particles.

3. Materials and methods

The aim of this chapter is to describe the materials employed in column transport tests and how they have been characterized. A brief assessment of the theoretical fundamentals behind some of the experimental methods is also included.

3.1 Porous medium

White quartz sand (Sigma-Aldrich, CA) in the 50-70 mesh (210-297μm) size range was used as the porous medium in this study. Sand was acid-treated following the procedure suggested by Torkzaban et al. [65]: the granular medium was soaked for 16 hours in a 70% (v/v) HNO_3 solution to remove possible traces of metal oxides and organic substances. Sand was then thoroughly rinsed with deionized water and sonicated for five 20-minutes cycles in water bath to raise the pH level. After every sonication cycle, deionized water was changed.

Scanning electron microscopy (SEM) confirmed the size values reported by the producer as shown in *Figure 3.1*. A median sand diameter of 250 μm was used for further calculations.

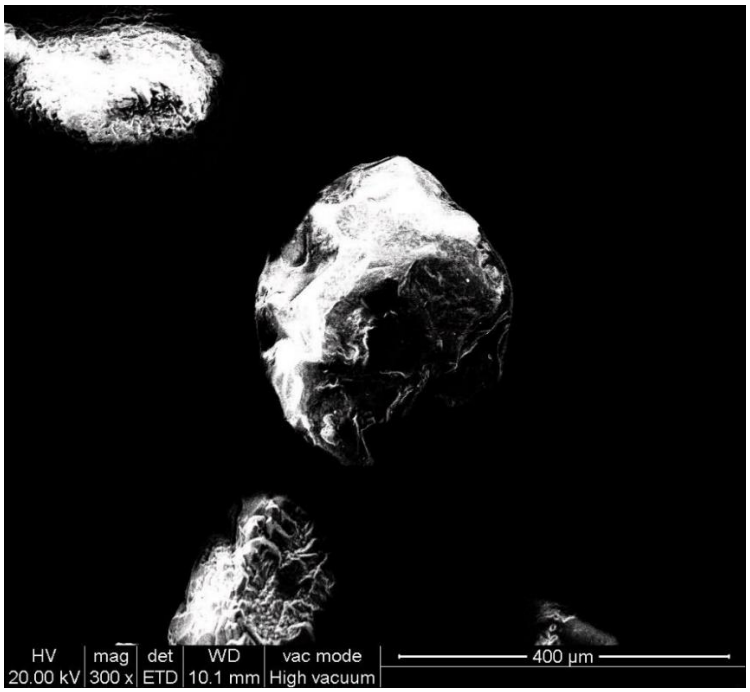

Figure 3.1: SEM image of white quartz sand grain

Electrophoretic mobility of sand grains was measured with Zetasizer Nano ZS (Malvern Instruments). Electrophoretic mobility of a particle suspended in a fluid domain is defined as the ratio between the particle velocity and the applied electric field, and can be correlated to surface potential by means of Henry's equation [66]:

$$\psi_0 = \frac{3\mu U_e}{2\varepsilon_0 \varepsilon_r f(ka_p)} \tag{3.1}$$

Where ψ_0 [M L^2 t^{-3} I^{-1}] is the surface potential, μ [M t^{-1} L^{-1}] is the fluid viscosity and $f(ka_p)$ is a correction factor, as listed in *Table 3.1*.

Table 3.1: Correction factors for Henry's equation

ka_p	0	1	2	3	4	5	10	25	100	∞
$f(ka_p)$	1	1.027	1.066	1.101	1.133	1.160	1.239	1.370	1.460	1.500

For values of ka_p typically found in colloids science, Henry's equation can be written with Smoluchowski's approximation as [67]:

$$\psi_0 = \frac{\mu U_e}{\varepsilon_0 \varepsilon_r} \tag{3.2}$$

For considerations mentioned in paragraph 2.1.1, measured electrophoretic mobilities are caused by surface charges at the shear plane and the potential calculated from Smoluchovski's equation is zeta-potential ψ_ζ. Zeta-potential values calculated as per equation (3.2) represent the difference of potential between the electrical double layer surrounding the particle and the dispersant medium at the shear plane [37].

Samples for electrophoretic mobility measurements were prepared by thoroughly milling sand grains and suspending the finer fraction in four NaCl solutions representative of ionic strengths employed in transport tests. Results are reported in *Table 3.2*.

Table 3.2: White quartz sand zeta-potential values at 1 mM, 10 mM, 100 mM and 1000 mM

Ionic strength I (mM)	Zeta-Potential ψ_ζ (mV)
1	-42
10	-37
100	-18.7
1000	-7.6

Measured ψ_ζ values are consistent with data found in literature [59,68,69] as absolute surface charge is expected to decrease with increasing ionic strength.

3.2 Nanoparticles

The behaviour of two types of silica nanoparticles was assessed in this study:

- Solid nanospheres obtained via a modified-Stöber [70] synthesis;
- Commercial hollow Matshperes, series 446 (Materium, CA)

Solid particles were selected due to their similar physical characteristics (e.g. density, Hamaker constant) as templates for mesoporous particles, that represent the real competitor to hollow spheres for applications as carriers or adsorbents.

3.2.1 Solid NPs

Transmission electron microscopy (TEM) was utilized to assess size and general morphology of solid NPs (*Figure 3.2*). Particles were found to be spherically shaped and with an average diameter of 170nm±10nm.

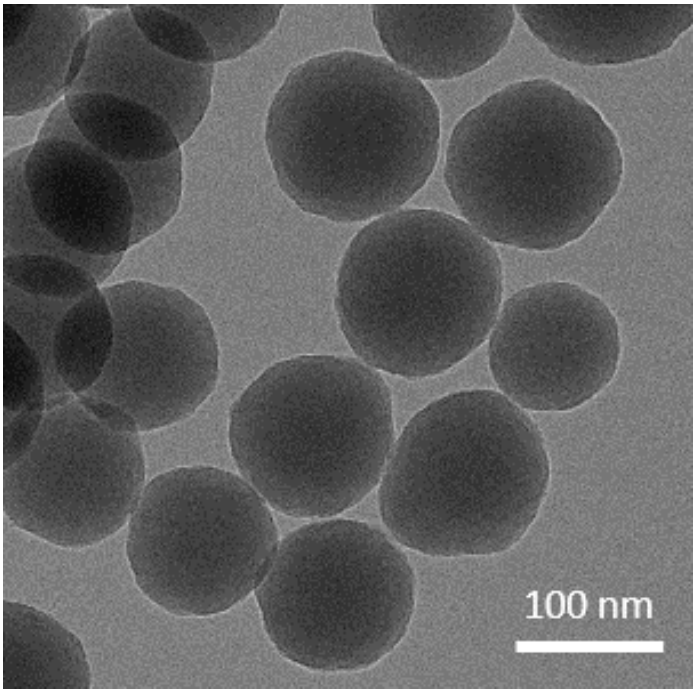

Figure 3.2: TEM image of solid SiO_2 NPs

Dynamic Light Scattering (DLS) measurements strongly confirmed TEM results as shown in *Figure 3.3*. Average diameter measured via DLS was 167nm, and size distribution analysis revealed an extremely high level of uniformity in the solid silica population, represented by a value of polydispersity index (PDI) equal to 0.04. In colloids and polymers science, polydispersity index is a dimensionless measure of the width of molecular weight or size distribution [71]. Its entity is scaled so that strongly uniform populations show values below 0.05 while samples with broad size distribution exhibit PDI over 0.7.

Solid silica NPs employed for DLS measurements were suspended in 10 mM NaCl solution at a concentration of 10 ppm.

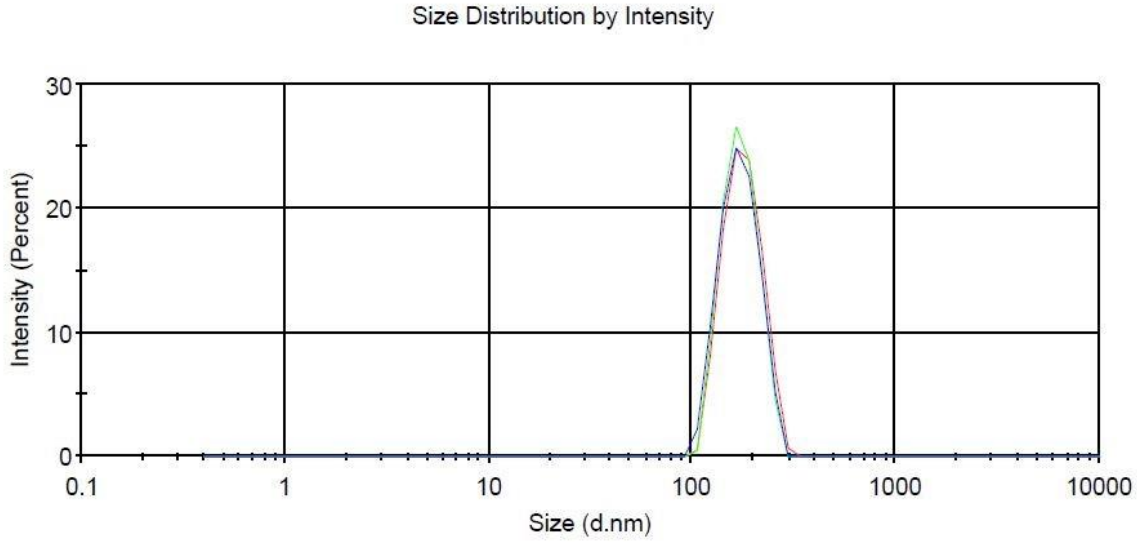

Figure 3.3: DLS – size distribution of solid SiO_2 NPs

Effects of pH on electrophoretic mobility were also evaluated: NaOH (1M) and HCl (100mM) solutions were used to correct the "natural" pH=5. Solid silica NPs were suspended in a 10 mM NaCl solution with a concentration of 10ppm. Results are shown in *Figure 3.4*.

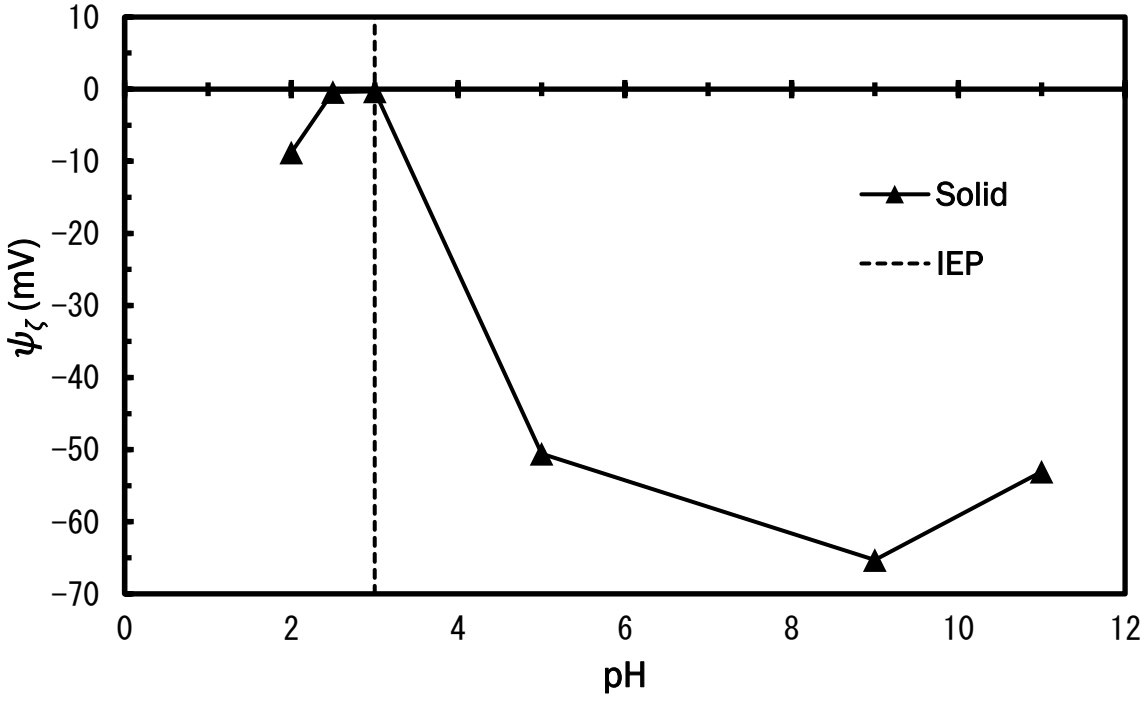

Figure 3.4: Effects of pH on Zeta potential for solid SiO_2 NPs

Effects of pH on surface properties are consistent with data found in literature [69]. The point of no charge (Isoelectric point IEP) was found to be in between pH=2.5 and pH=3. ψ_ζ of NPs suspension at natural pH was -50 mV. Solid spheres' strongly negative surface charge resulted in high stability of the suspension (more on that in the following chapter).

3.2.2 Hollow NPs

Commercial hollow Matspheres, series 446 (Materium, Ca) were used as hollow silica particles. TEM analysis revealed spherically-shaped particles with average diameter of 240nm±15nm (*Figure 3.5*).

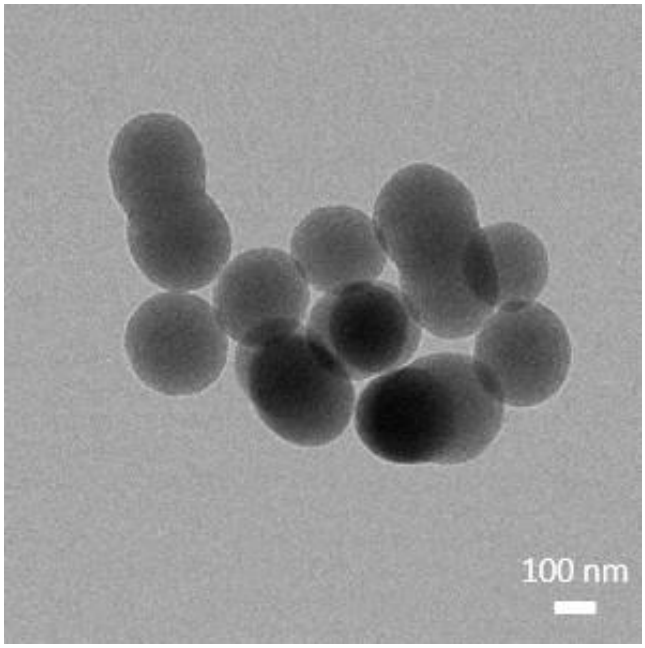

Figure 3.5: TEM image of hollow SiO_2 NPs

TEM measurements of hollow spheres were considered inconclusive regarding the thickness of the silica shell and disc centrifuge analysis was employed for further evaluations. Disc centrifuge operation is based on Stokes' law [72]:

$$v_{stokes} = \frac{g\left(\rho_p - \rho_f\right) {d_p}^2}{18\mu} \tag{3.3}$$

where v_{stokes} [L t^{-1}] is the Stokes' final settling velocity.

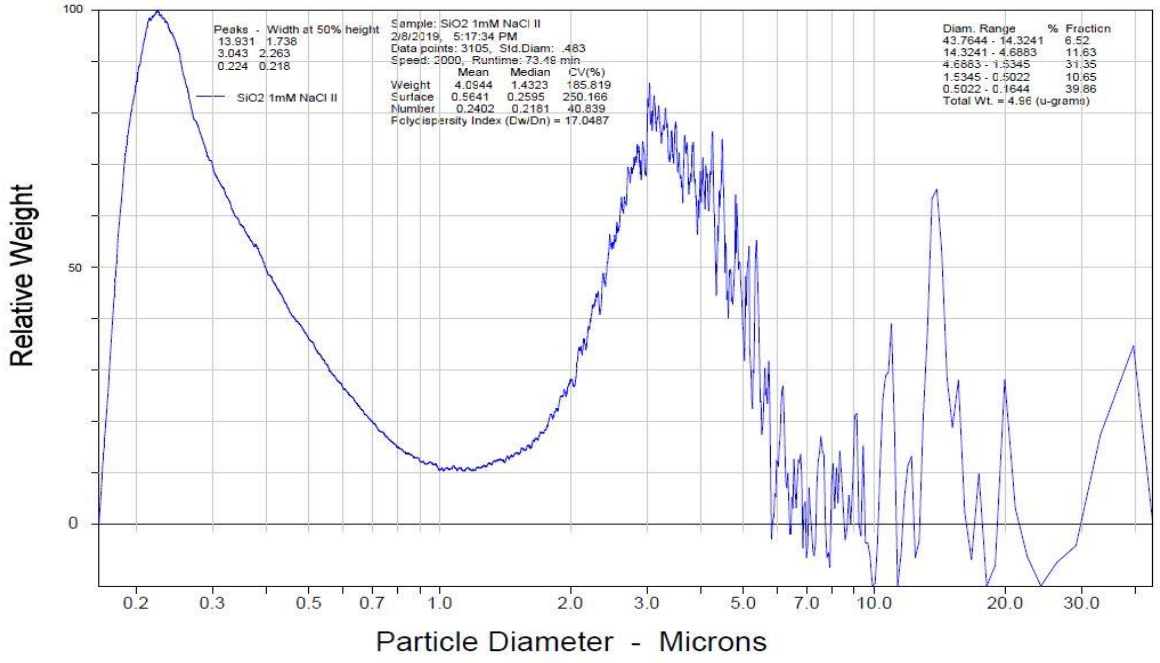

Figure 3.6: Disc centrifuge - hollow SiO_2 size distribution by weight

Hollow spheres' density was evaluated from measured sedimentation velocities for particles of the size measured by TEM. A density of 1.8 g/cm^3, corresponding to a silica shell of 25 nm, was found to match disc centrifuge data with TEM. Dimensional analysis revealed a particle distribution with very low uniformity: the bimodal behaviour reported in *Figure 3.6* suggests the significant presence, in terms of weight, of a coarser particles population undetected by TEM within the commercial product.

Hollow silica NPs employed for disc centrifuge analysis were suspended in 1 mM NaCl solution at a concentration of 500 ppm.

The presence of micro-sized particles was confirmed by SEM as reported in *Figure 3.7*.

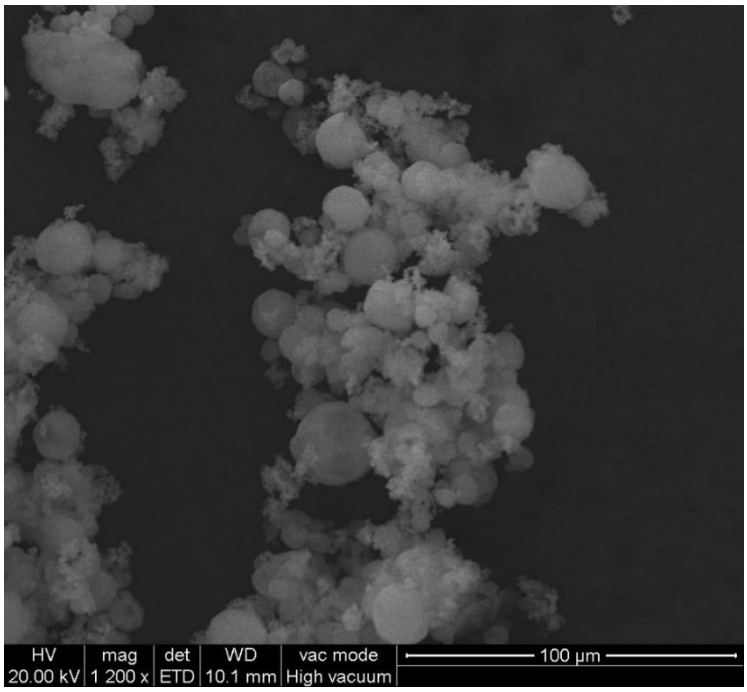

Figure 3.7: SEM image of hollow SiO_2 NPs

DLS measurements provided further confirmation regarding the small population's size distribution (*Figure 3.8*). The average diameter measured by DLS was 246nm.

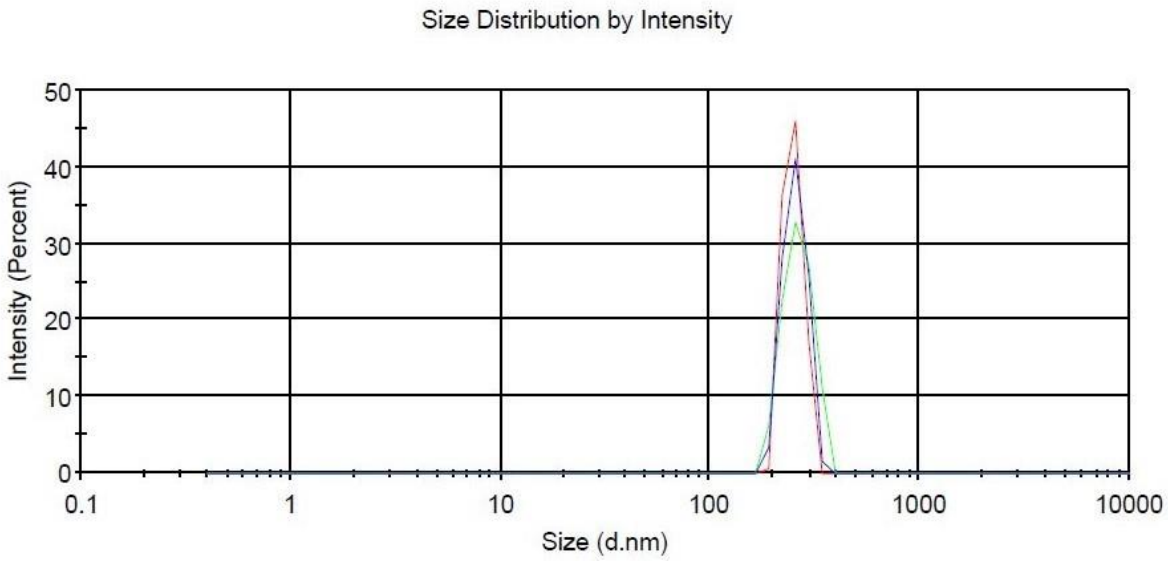

Figure 3.8: DLS – size distribution of hollow SiO_2 NPs

An average diameter of 250 nm with a silica shell of 25 nm was used for further calculations on the small population of hollow silica NPs.

Surface properties at varying pH were assessed in the same conditions used for solid particles (*Figure 3.9*). IEP was found at pH=4. Hollow particles were very weakly negatively charged at "natural" pH=5.8.

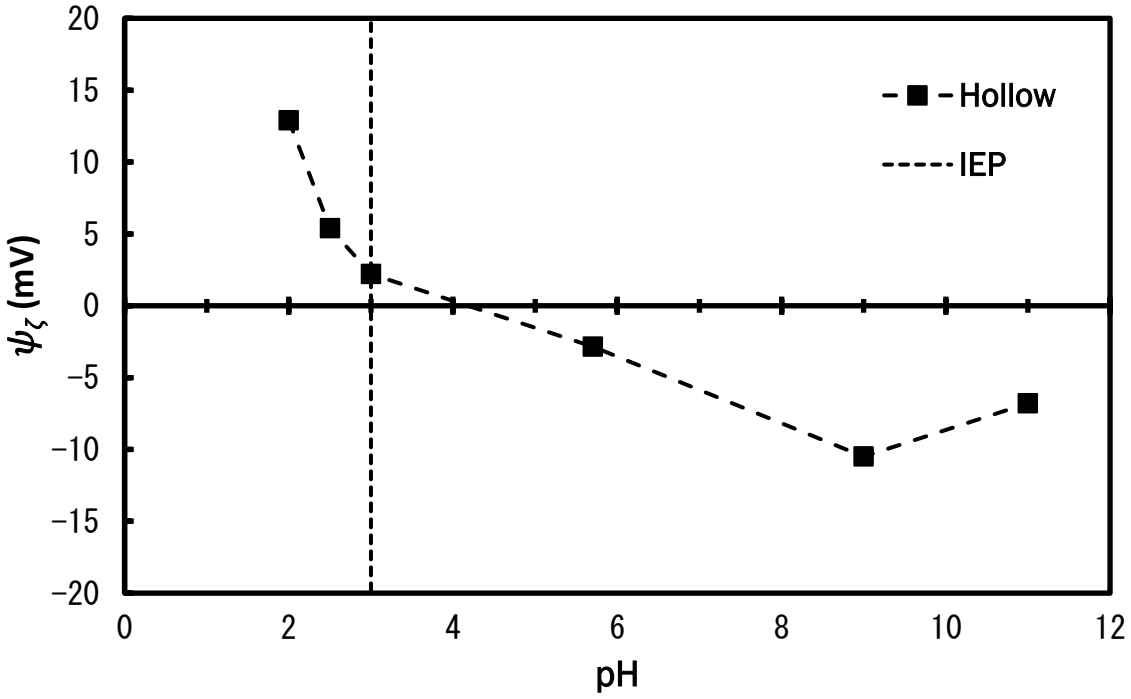

Figure 3.9: Effects of pH on Zeta potential for hollow SiO_2 NPs

3.3 Column transport experiments

A schematic view of the experimental setup utilized to conduct transport tests is reported in *Figure 3.10*. Suspensions were injected via a peristaltic pump (Cole-Palmer, Masterflex L/S, model 77200-12, CA) with a flow rate of 1 ml/min in water saturated sand-packed column (Chromaflex, Fisher, CA, 1.0 cm i.d., and 10 cm length). Electrolyte and SiO_2 NPs concentrations at the outlet of the column were measured by UV-Vis spectroscopy (Agilent Technologies, Model 8453) in a quartz flow-cell (Hellma Analytics, GE, 10 mm pathlength, 300 µl volume).

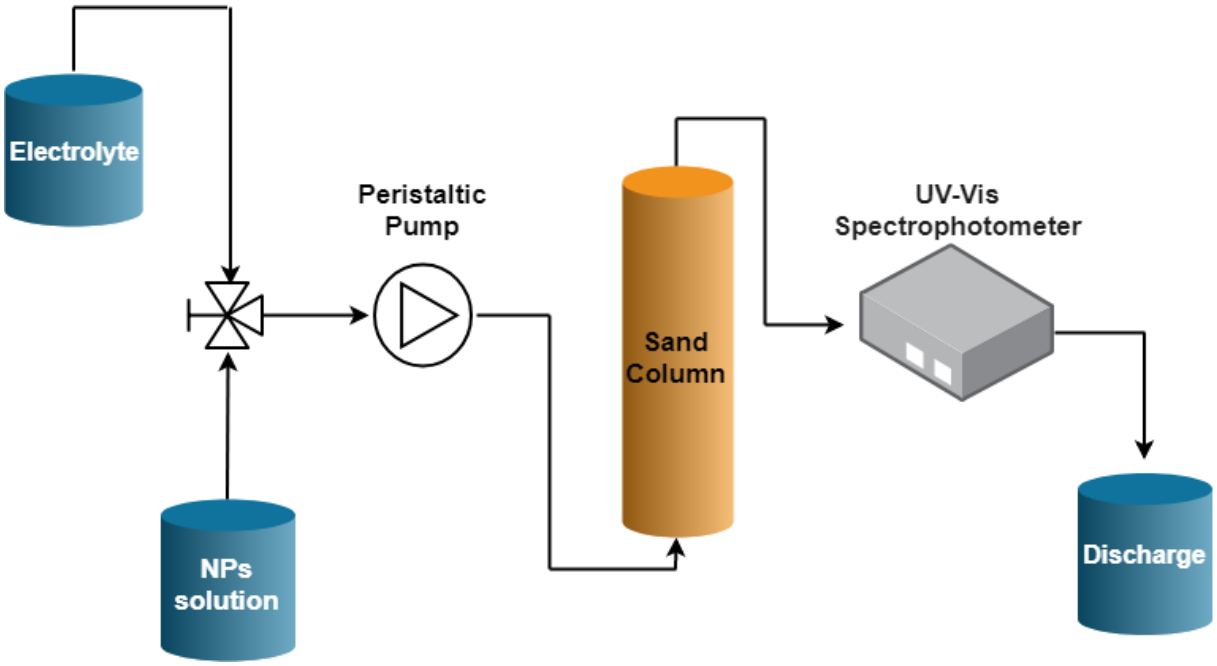

Figure 3.10: Schematic view of transport test setup

Acid-treated sand was subjected to three 20-minutes sonication cycles in deionized water bath to minimize possible releases of nanoscale material that could interfere with NPs detection during injections. Deionized water containing finer sand fraction was changed after every sonication cycle.

The glass column was wet-packed following the procedure suggested by Oliveira et al. [73]: 1-cm layers of sand were deposited in water and the column was then vibrated for 20 seconds to achieve homogeneous and reproducible packing conditions. This operation was repeated until the obtainment of a final bed's length of 10 cm.

NPs suspensions were sonicated for at least 40 minutes before injection: special care was paid during sonication to avoid the increase of temperature inside the water bath beyond 40°C.

NaCl was used as the electrolyte: transport tests for hollow particles were conducted at ionic strengths of 1 mM and 10 mM, while solid NPs, as a result of their greater stability, were injected at 1 mM, 10 mM, 100 mM and 1 M electrolyte concentrations. To estimate hydrodynamic parameters of the porous medium, a tracer test was carried out before every particles injection: NaCl (1 M) was used as the tracer due to its non-reactivity, as suggested by many authors [62,65,69].

Transport tests were carried out injecting:

- 3 pore volumes (PV) of deionized water to verify the absence of material released from the porous medium. In this phase, the "blank" spectrum used for reference was also measured;
- 4 PV of 1M NaCl solution for tracer test;
- 5 PV of particle-free electrolyte solution at the specific concentration employed for each test;
- at least 6 PV of particles suspended in the same initial solution chemistry. Hollow and solid particles were injected respectively with an initial concentration of 500 ppm and 100 ppm;
- 3 PV of particle-free electrolyte solution;
- 3 PV of particle-free electrolyte solution at reduced ionic strength to promote eventual releases of particles;
- 3 PV of deionized water;

For tests conducted at 1 mM salt concentration, the injection of electrolyte solution at reduced ionic strength was not carried out. For tests at 100 mM and 1 M, a reduced ionic strength of 10 mM was chosen for intermediate post-flushing.

Ultraviolet-visible (UV-Vis) spectroscopy is an analytical technique that measures absorbance of light [74]. It's based on electronic transitions of molecules absorbing lights that excite electrons from lower energy orbital to a higher energy unoccupied orbital: the relation between absorbed light and suspended NPs' concentration is given by Beer-Lambert law [75]:

$$A = \zeta \, l \, C \tag{3.4}$$

being A the light absorbance, l [L] the cell pathlength and ζ [M^{-1} L^2] the absorbivity coefficient characteristic to every material. Light absorbance is measured with respect to a "blank" reference.

Linear correlation was verified measuring absorbance values at known NPs and NaCl concentrations. Silica NPs and sodium chloride were detected respectively at a wavelength of 350 nm and 205 nm. Calibration curves are shown in *Figure 3.11*, *Figure 3.12* and *Figure 3.13*.

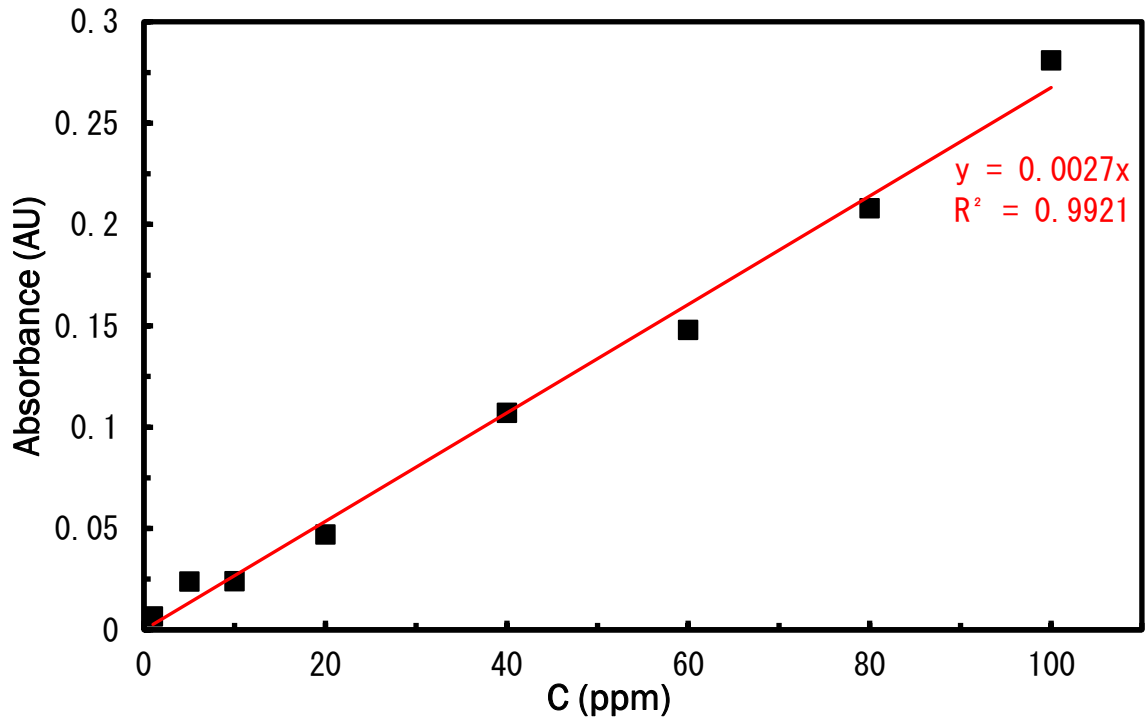

Figure 3.11: UV-Vis calibration curve for solid SiO_2 NPs

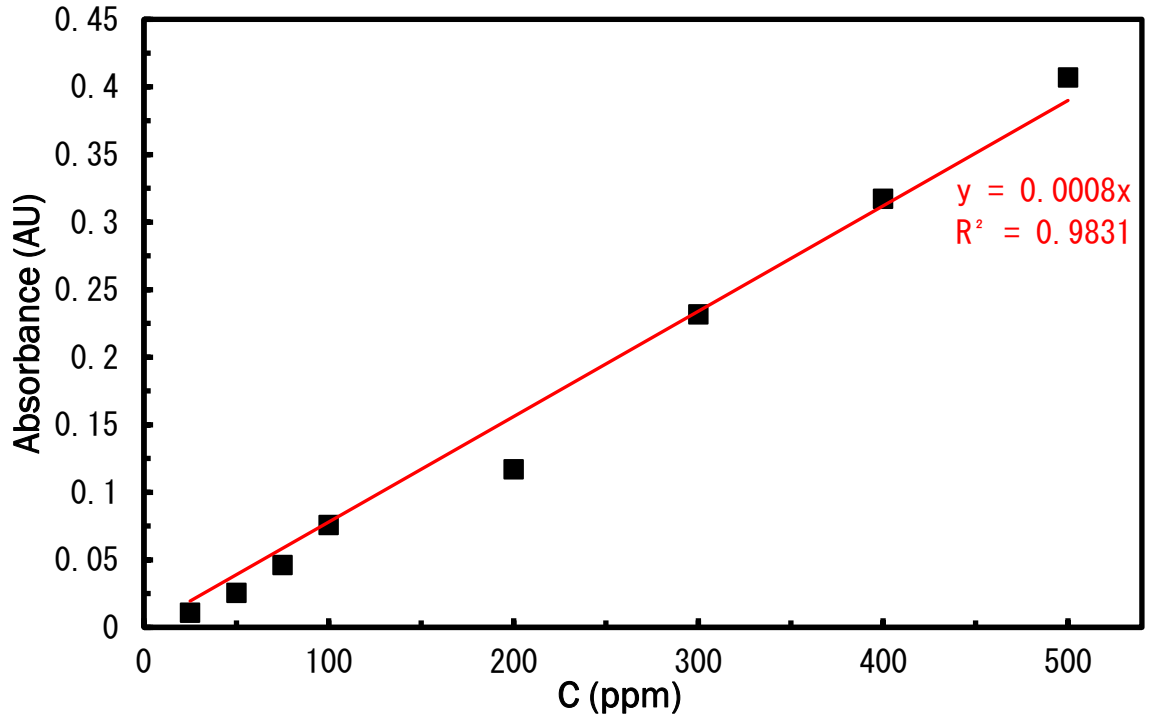

Figure 3.12: UV-Vis calibration curve for hollow SiO_2 NPs

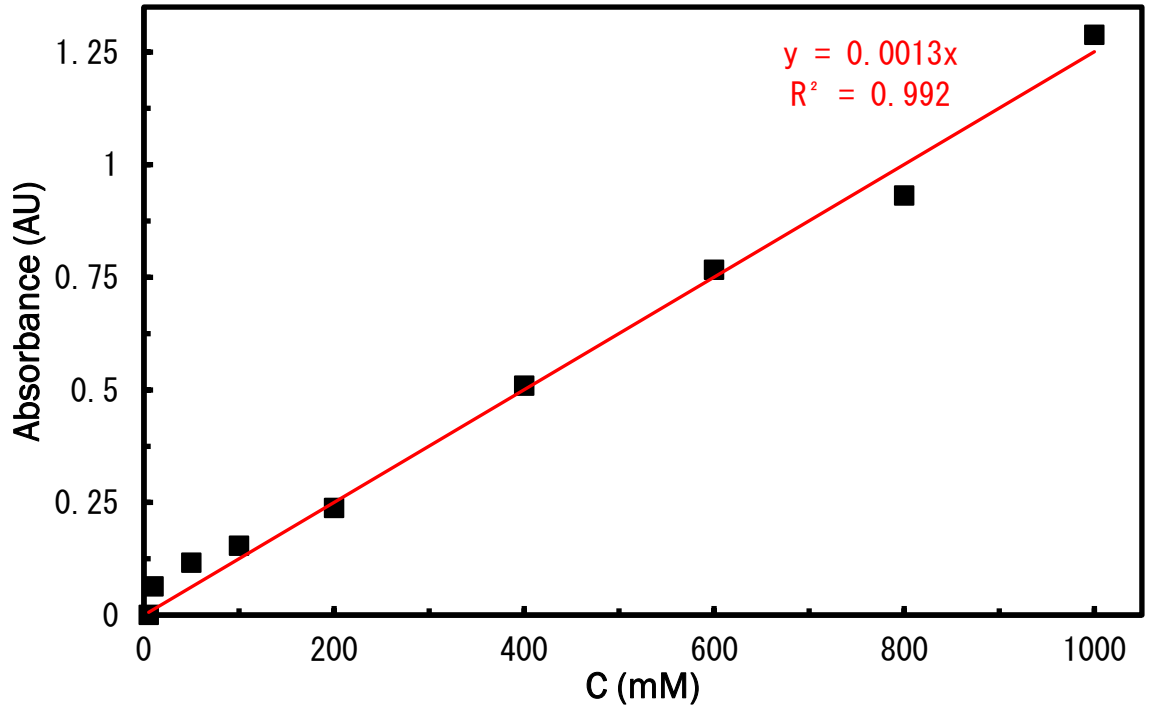

Figure 3.13: UV-Vis calibration curve for NaCl

Results showed good linearity between NPs and NaCl concentrations and absorbance.

4. Results

In this chapter, calculations of DLVO interaction energies and single collector contact efficiencies based on the results of characterization are presented alongside BTCs from column transport tests and possible solutions to macro-scale modelling.

4.1 Calculations

4.1.1 DLVO interaction profiles

DLVO energy profiles in sphere-sphere and sphere-plate geometries were calculated for solid and hollow SiO_2 NPs (see paragraph 2.1.1 for reference). A summary of the values of physical properties used for DLVO calculations is shown in *Table 4.1*. Despite having the same composition, differences in the crystalline structure of SiO_2 NPs and white quartz sand result in different physical properties [76].

Table 4.1: Physical properties of silicon dioxide, water and white quartz sand at 100nm

Medium	Refractive index δ	Relative dielectric constant ε
SiO_2	1.489	3.9
White quartz sand	1.51	4.2
Water	1.33	78.5

Interaction profiles for solid SiO_2 NPs in sphere-sphere and sphere-plate geometries are shown respectively in *Figure 4.1* and *Figure 4.2* and were calculated for a temperature of 293 K.

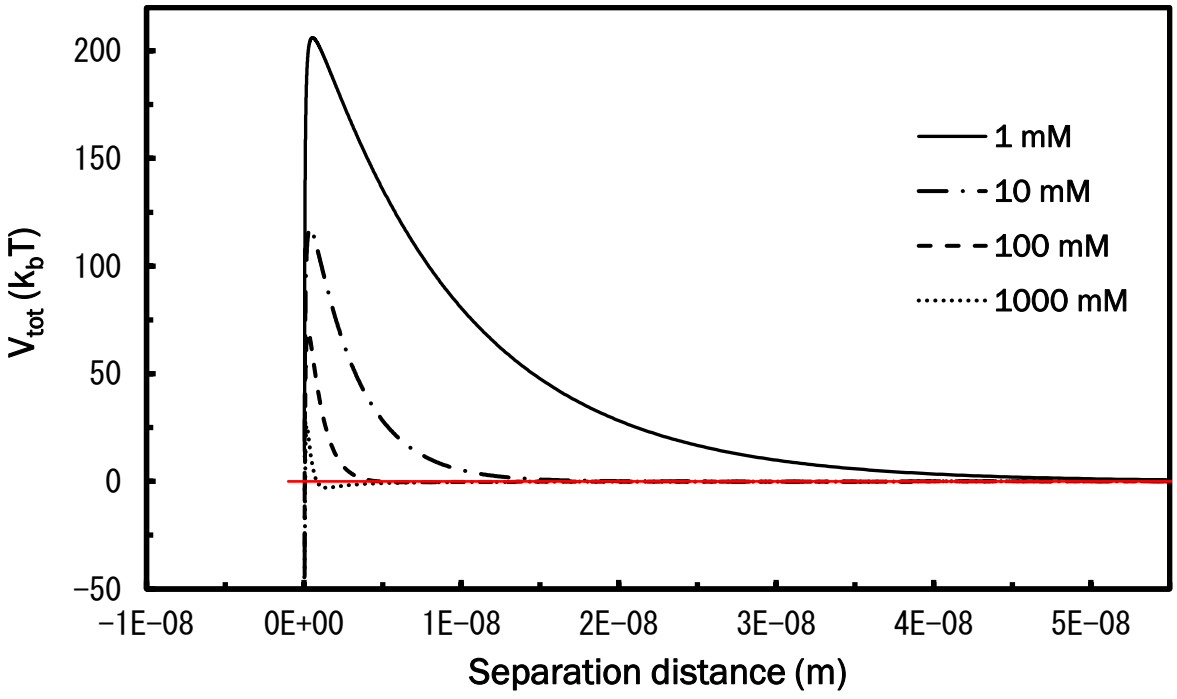

Figure 4.1: DLVO particle-particle interaction profiles for solid SiO_2 NPs

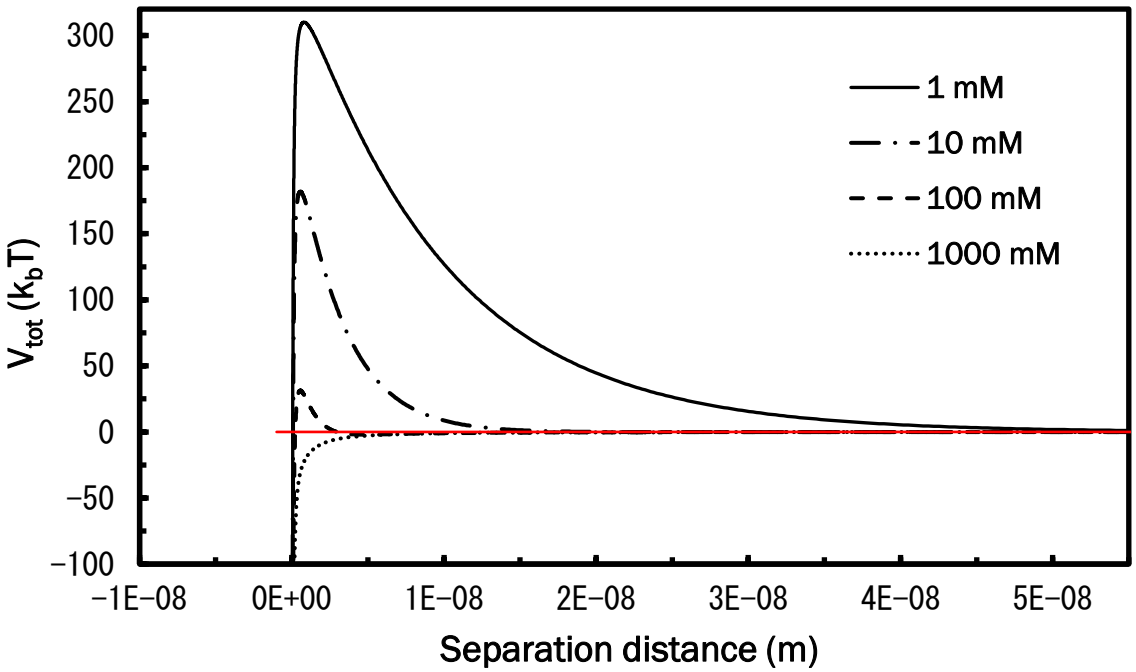

Figure 4.2: DLVO particle-collector interaction profiles for solid SiO_2 NPs

As a result of their strongly charged surface, sphere-sphere interaction profiles exhibit high energy barriers and the absence of secondary wells at ionic strengths of 1 mM, 10 mM and 100 mM: in such conditions, aggregation is negligible and suspensions are stable. In 1 M NaCl solutions, solid particles can aggregate in a secondary minimum.

In particle-collector geometry, strongly repulsive interactions occur at 1 mM and 10 mM; in these conditions, NPs can travel long distances in groundwater environments. In 100 mM NaCl solutions, particles can be retained by the porous medium in a secondary minimum at a distance of ≈ 5nm from the sand grain. For ionic strengths of 1 M, favourable deposition conditions are completely developed and particles are likely to attach to the collector's surface at every contact.

Magnitude of typical features of DLVO interaction profiles for solid SiO_2 NPs are summarized in *Table 4.2*. Depth of primary minima (Φ_{min}), height of energy barriers (Φ_{max}) and depth of secondary wells (Φ_{sec}) are expressed as k_bT. For DLVO calculations accounting only for double layer and Van der Waals interactions, as separation distance between surfaces approaches zero, total potential tends to -∞. Nonetheless, values of total potential at separation distances of 3×10^{-11} m were used as approximate estimation of Φ_{min} only for comparative purposes.

Table 4.2: Φ_{min}, Φ_{max} and Φ_{sec} of solid SiO_2 NPs at 1 mM, 10 mM, 100 mM and 1 M

I (mM)	Particle-Particle (k_bT)			Particle-Collector (k_bT)		
	Φ_{min}	Φ_{max}	Φ_{sec}	Φ_{min}	Φ_{max}	Φ_{sec}
1	/	206.0	/	-362.4	310.1	/
10	-65.0	117.4	/	-464.3	181.9	/
100	-95.2	69.6	/	-605.5	31.3	-2.1
1000	-113	25.8	-2.9	-682	/	/

Interactions profiles of hollow SiO_2 NPs in sphere-sphere and sphere-plate geometries are reported respectively in *Figure 4.3* and *Figure 4.4*. Since characterization results of hollow SiO_2 NPs were inconclusive regarding the dimensions of the micro-sized population contained in the commercial product, *Figure 4.3* and *Figure 4.4* have to be considered representative just of the interactions profiles of the small population (250 nm, silica shell of 25 nm).

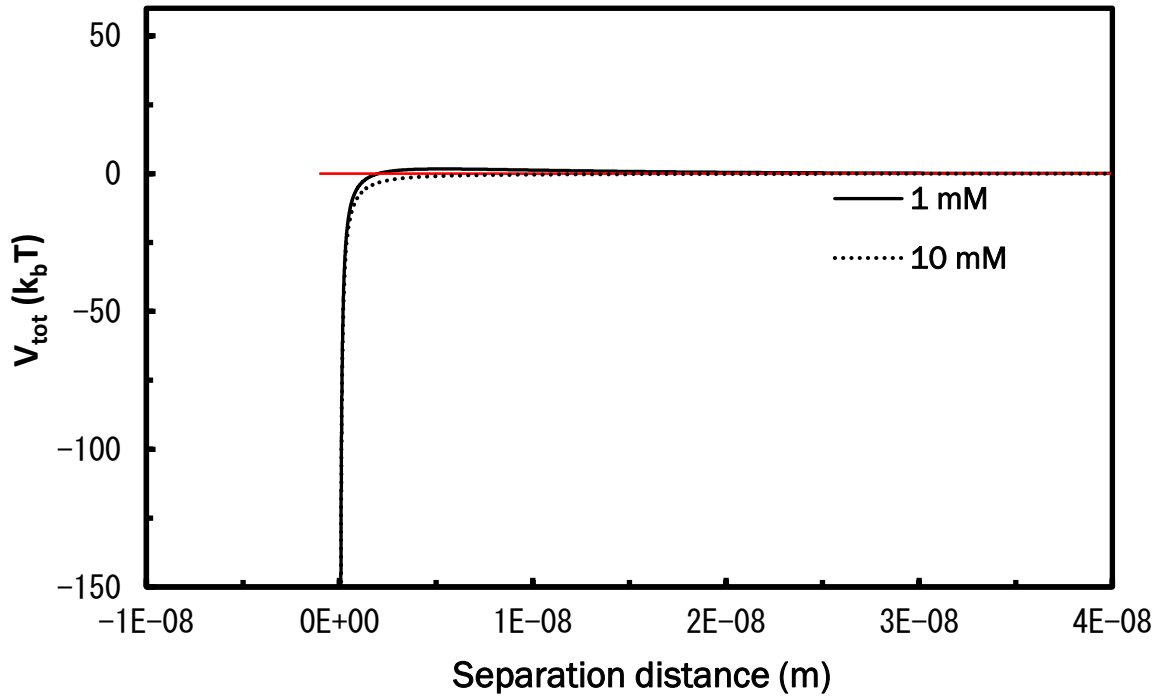

Figure 4.3: DLVO particle-particle interaction profiles for hollow SiO_2 NPs

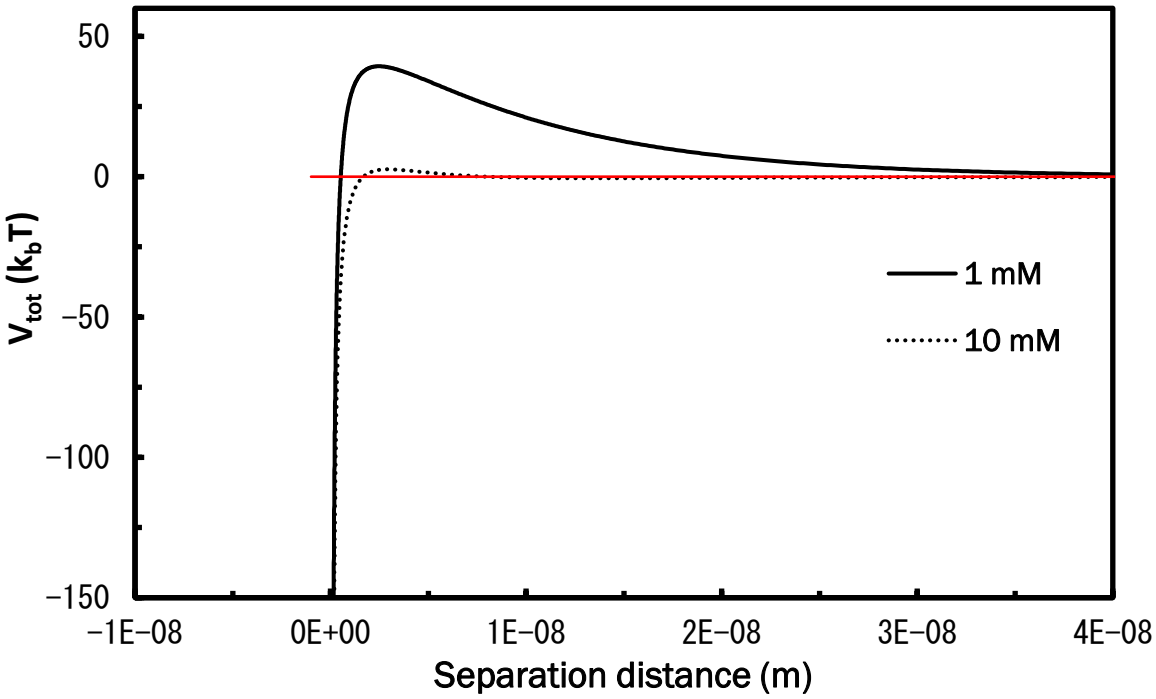

Figure 4.4: DLVO particle-collector interaction profile for hollow SiO_2 NPs

Due to their weakly charged surfaces, hollow particles' sphere-sphere interaction profiles exhibit favourable aggregation conditions at both 1 mM and 10 mM salt concentrations. Hollow silica NPs required intensive sonication (1h) before the injection in the sand-packed column.

Significant energy barriers arise when hollow particles try to attach to the sand grain as a result of the collector's surface charge both at 1 mM and 10 mM electrolyte concentrations; the magnitude of repulsion forces, as expected, decreases with increasing ionic strength. A shallow secondary minimum can also be observed for the interaction profile at a salt concentration of 10 mM.

Depths of primary minima (Φ_{min}), heights of energy barriers (Φ_{max}) and depths of secondary wells (Φ_{sec}) for hollow particles interactions are reported in *Table 4.3*.

Table 4.3: Φ_{min}, Φ_{max} and Φ_{sec} of hollow SiO_2 NPs at 1 mM and 10 mM

I(mM)	Particle-Particle (k_bT)			Particle-Collector (k_bT)		
	Φ_{min}	Φ_{max}	Φ_{sec}	Φ_{min}	Φ_{max}	Φ_{sec}
1	-312.5	1.7	/	-1004.0	39.4	/
10	-316.1	/	/	-1039.7	2.7	-0.5

Differences in calculated DLVO profiles of hollow and solid silica NPs are mostly imputable to different surface properties. To better assess the influence of the cavity on DLVO interactions, further calculations were carried out assuming same zeta potential values for the two sets of particles in sphere-plate geometry (zeta potentials of SiO_2 NPs and sand grains for following calculations are the same used to obtain *Figure 4.2*).

The influence of the inner sphere's dimension was evaluated for two "ideal" silica particles with outer diameters of 250 nm and 25 nm. In particular, typical DLVO features of hollow particles ($\Phi_{min}(h)$, $\Phi_{max}(h)$, $\Phi_{sec}(h)$) were compared to their respective for solid NPs ($\Phi_{min}(s)$, $\Phi_{max}(s)$, $\Phi_{sec}(s)$) at different a_{is}/a_p ratios, being a_{is} the radius of the inner sphere.

Results for the 250 nm and 25 nm particles are reported respectively in *Figure 4.5* and *Figure 4.6*. All profiles showed the same "shape" of *Figure 4.2*: at 1 mM and 10 mM high energy barriers and an absence of secondary wells were observed, while at 1 M the profiles showed no repulsive interaction. At 100 mM, smaller repulsive barriers and shallow secondary minima were found.

For the bigger particle (250 nm), the presence of the inner sphere marginally influenced the depth of the primary minima at high a_{is}/a_p ratios, while no effects were found on energy barriers and secondary minima. The presence of the cavity adds a repulsive contribution to the DLVO profile, thus leading to an absolute reduction of the depth of primary minima $\left(\frac{\Phi_{min}(h)}{\Phi_{min}(s)} < 1\right)$ as the a_{is}/a_p ratio increases.

For the smaller particle (25 nm), inner sphere showed significant influence also on energy barriers and secondary minima: effects included the absolute reduction of both primary and secondary wells $\left(\frac{\Phi_{min}(h)}{\Phi_{min}(s)} < 1, \frac{\Phi_{sec}(h)}{\Phi_{sec}(s)} < 1\right)$ and the increase of the repulsive barrier $\left(\frac{\Phi_{max}(hollow)}{\Phi_{max}(solid)} > 1\right)$ at high a_{is}/a_p ratios.

Calculations show that for the case of study (a_{is}/a_p=0.8, d_p=250 nm), the influence of the inner sphere is neglectable and differences in DLVO profiles between hollow and solid particles are almost exclusively due to surface properties.

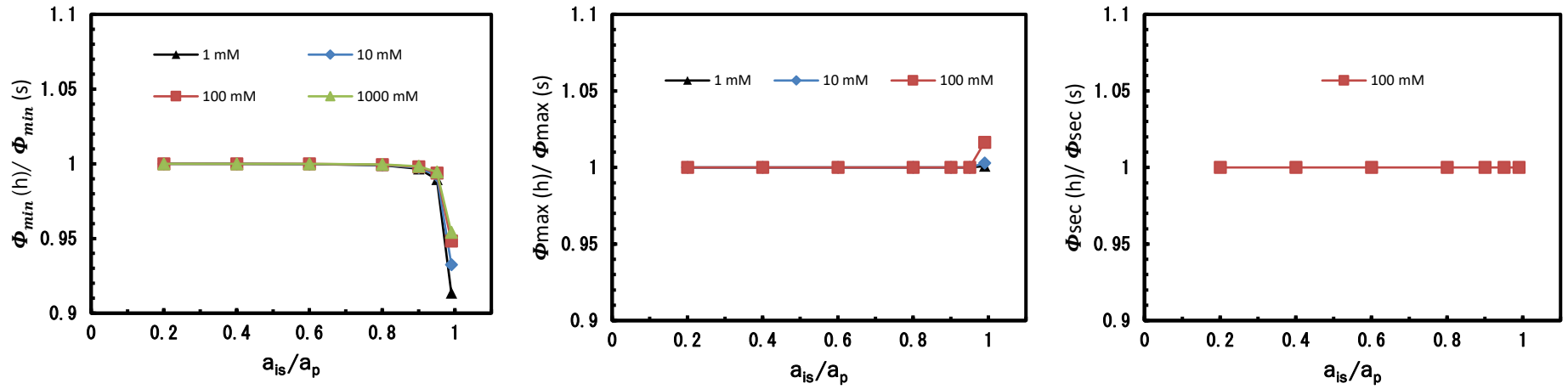

Figure 4.5: Influence of inner sphere's radius on Φ_{min}, Φ_{max} and Φ_{sec} in particle-collector interactions for outer sphere's diameter of 250 nm

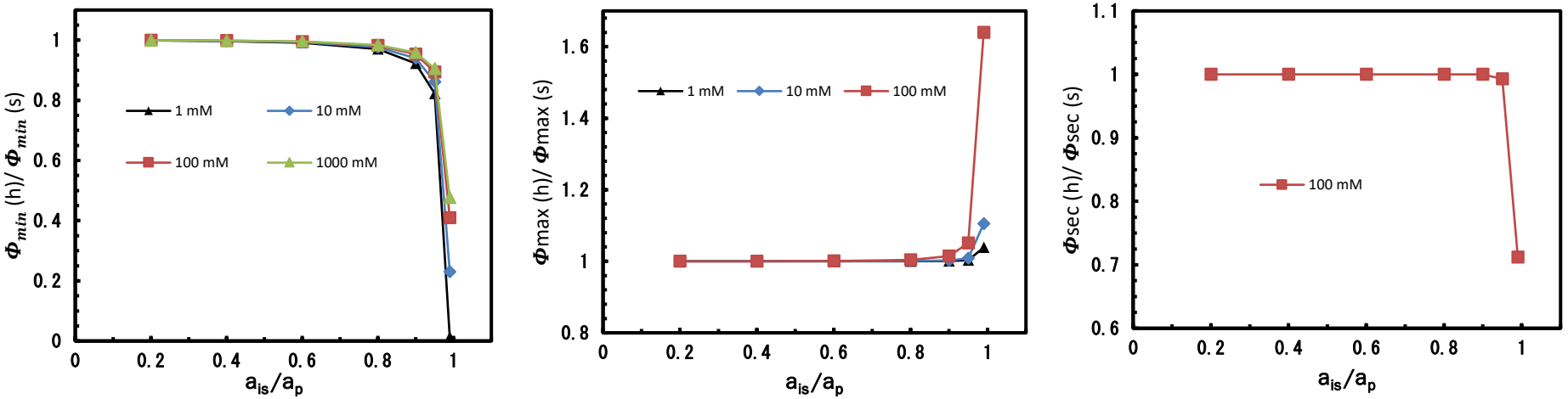

Figure 4.6: Influence of inner sphere's radius on Φ_{min}, Φ_{max} and Φ_{sec} in particle-collector interactions for outer sphere's diameter of 25 nm

4.1.2 Single collector contact efficiencies

Single collector contact efficiencies as a function of particles size were calculated for hollow and solid particles as per paragraph 2.1.2. Values employed for calculations are reported in *Table 4.4.* Results are reported in *Figure 4.7* and *Figure 4.8*.

Table 4.4: Values of parameters employed for prediction of single collector contact efficiency

Parameter	Solid NPs	Hollow NPs
Pore-water velocity (m/s)	5.6×10^{-4}	5.6×10^{-4}
Porous medium porosity (-)	0.4	0.4
Collector diameter (m)	2.5×10^{-4}	2.5×10^{-4}
Particle density (g/cm³)	2.65	1.8
Fluid density (g/cm³)	1	1
Fluid viscosity (Pa s)	1×10^{-3}	1×10^{-3}
Fluid temperature (K)	293	293
Global Hamaker constant H_{132} (J)	6.59×10^{-21}	5.79×10^{-21}

Global Hamaker constants were estimated as per equation (2.4). Physical properties of the hollow particles were obtained by a weighted average of the properties of the filling medium (water) and the silica shell (note that a global Hamaker constant accounting for the cavity is not required for calculations of DLVO profiles, as the influence of the inner sphere is estimated with an additional Van der Waals contribution).

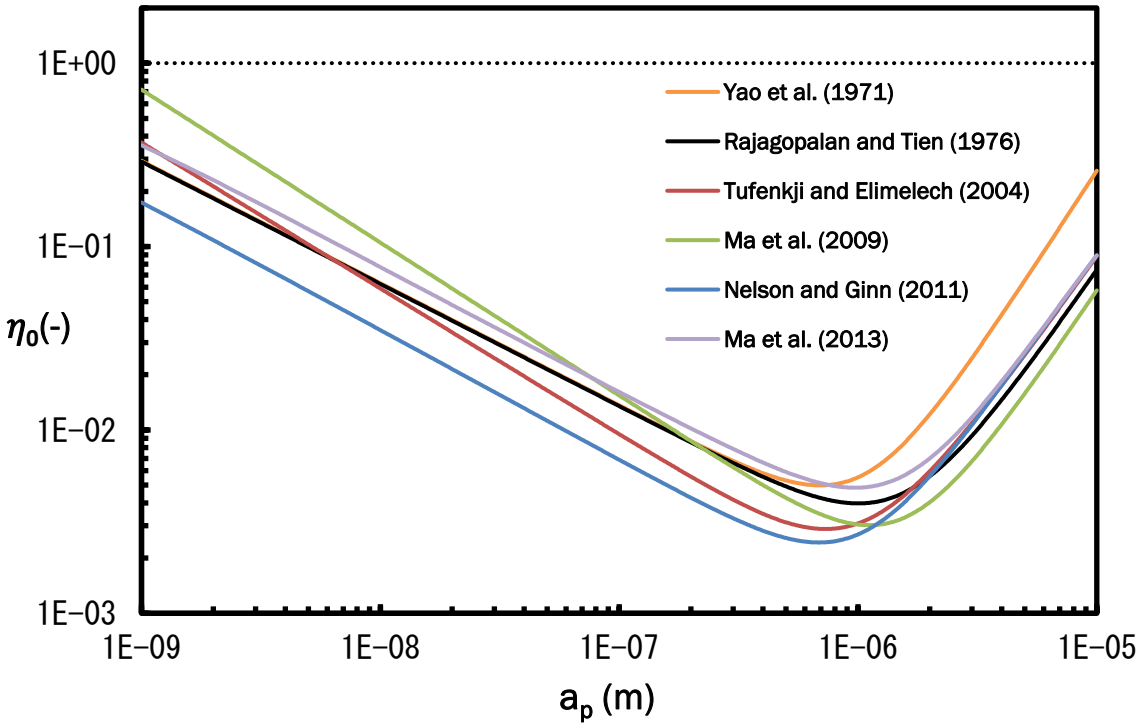

Figure 4.7: Single collector contact efficiency as a function of particle size for solid SiO_2 NPs

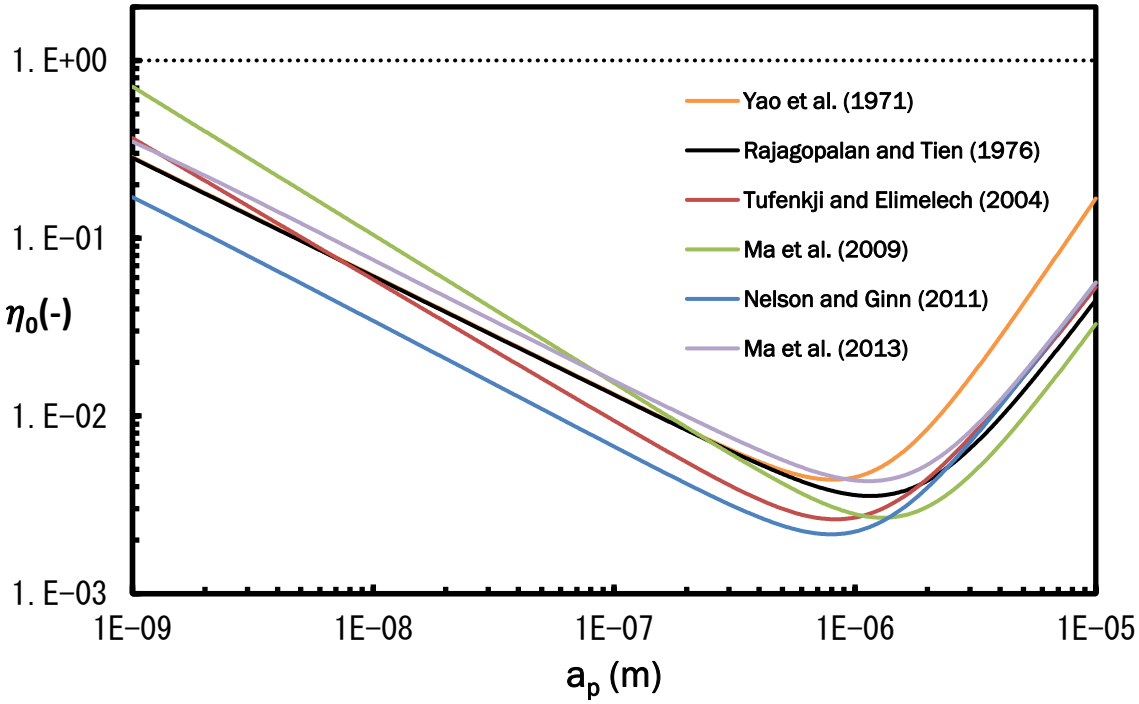

Figure 4.8: Single collector contact efficiency as a function of particle size for hollow SiO_2 NPs

Flow conditions were found to be unfavourable to particles' collision with the collector for the diameters of interest: average single collection efficiencies for hollow (a_p=125 nm) and solid (a_p=85 nm) SiO_2 NPs were respectively 1.04% and 1.40%.

For the reasons expressed in paragraph 4.1.1, *Figure 4.8* has to be considered representative just of the behaviour of the population of small silica NPs (250 nm, silica shell of 25 nm).

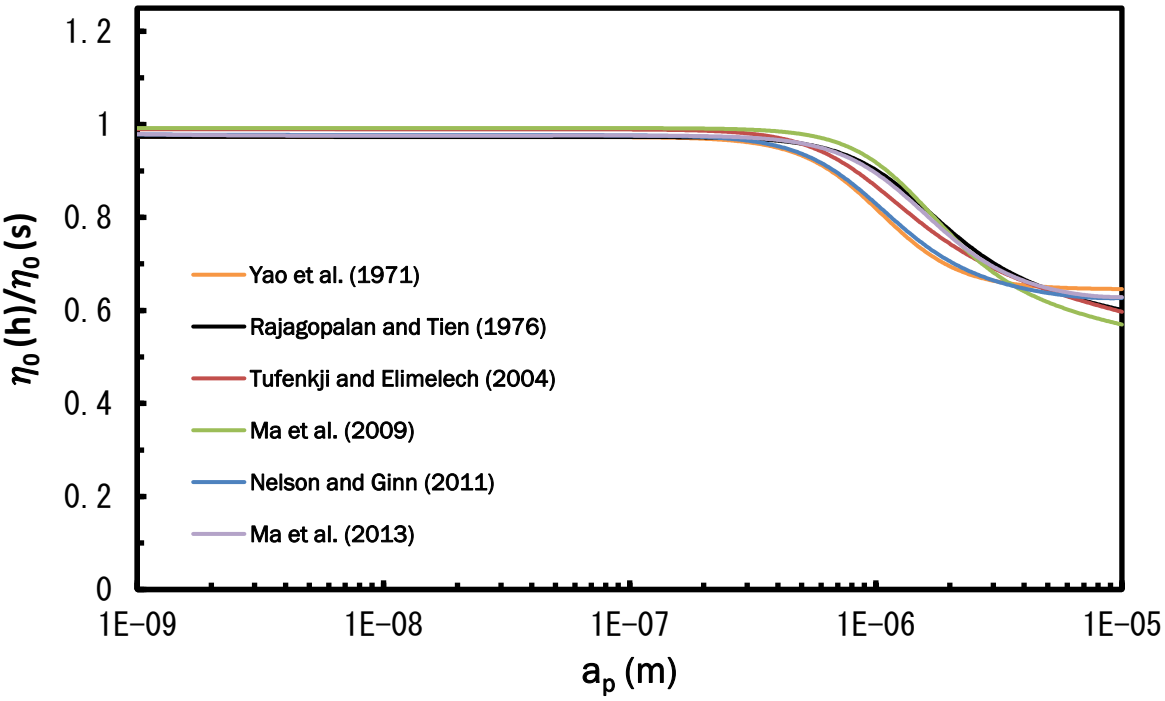

Figure 4.9: Ratio of η_0 for hollow and solid SiO_2 NPs as a function of particles size

To eliminate the effect of different sizes, the ratio between contact efficiencies of hollow (η_0(h)) and solid (η_0(s)) NPs was plotted as a function of particle's size (*Figure 4.9*).

As a result of smaller Hamaker constant and density, hollow particles exhibit less probability of colliding with the sand grain compared to solid particles $\left(\frac{\eta_0(\mathrm{h})}{\eta_0(\mathrm{s})} < 1\right)$ throughout the whole dimensional range usually considered in colloids science.

When gravitational effects dominate, the density difference between the two sets of particles produces a significant reduction in predicted contact efficiency for hollow particles ($\eta_0(\mathrm{h}) \approx 0.61\,\eta_0(\mathrm{s})$ for a_p=10 μm). On the contrary, the marginal difference of Hamaker constant between the two sets of particles doesn't result in a relevant decrease of the contact efficiency of the hollow NPs, even for small sizes ($\eta_0(\mathrm{h}) \approx 0.98\,\eta_0(\mathrm{s})$ for a_p=1 nm).

4.2 Breakthrough curves

Experimental BTCs of solid and hollow SiO_2 NPs at ionic strength of 1 mM and 10 mM are reported in *Figure 4.10* and *Figure 4.11*.

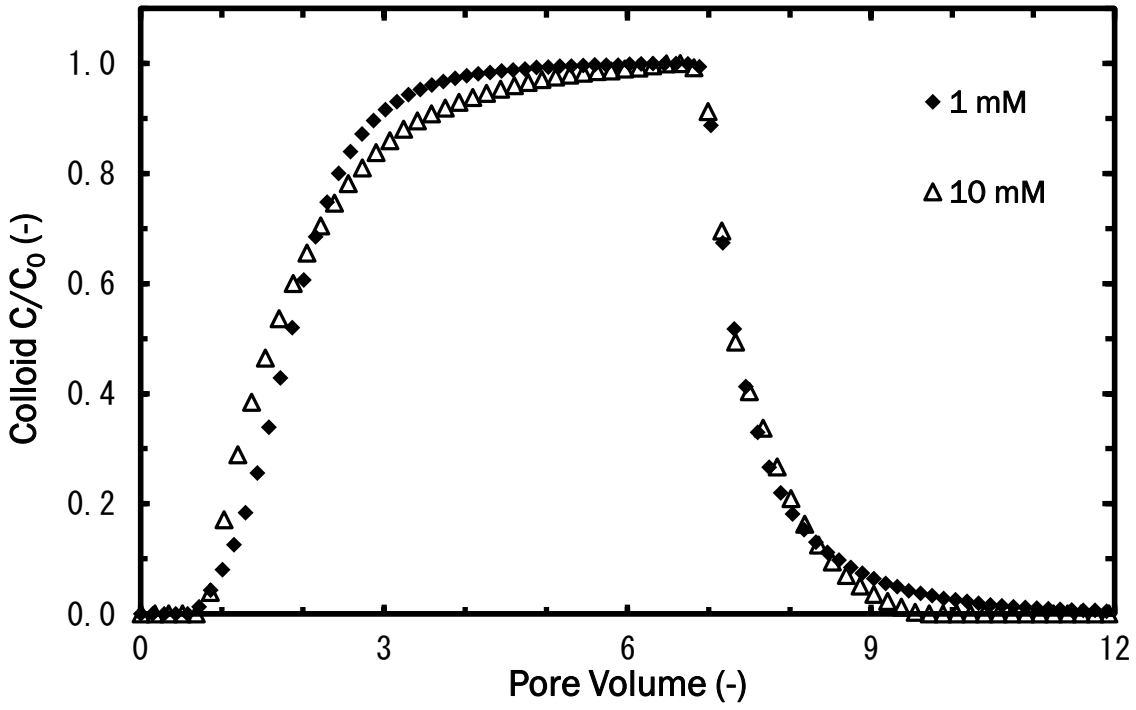

Figure 4.10: Observed BTCs of solid SiO_2 NPs in 1 mM and 10 mM NaCl solution

As expected from DLVO and single collector contact efficiency calculations, solid NPs showed high mobility in both 1 mM and 10 mM NaCl solutions and were able to reach $\mathrm{C}/\mathrm{C}_0 \approx 1$ after 5 pore volumes (PV) from the time of initial injection.

Lesser repulsive forces for particle-collector interaction resulted in higher retention of hollow SiO_2 NPs compared to solid NPs at both electrolyte concentrations: in 1 mM solutions, C/C_0 reached values of ≈ 0.8 after 5 PV. For ionic strength of 10 mM no plateau was reached even after 8 injected PV and normalized colloid concentration reached a maximum value of ≈ 0.6.

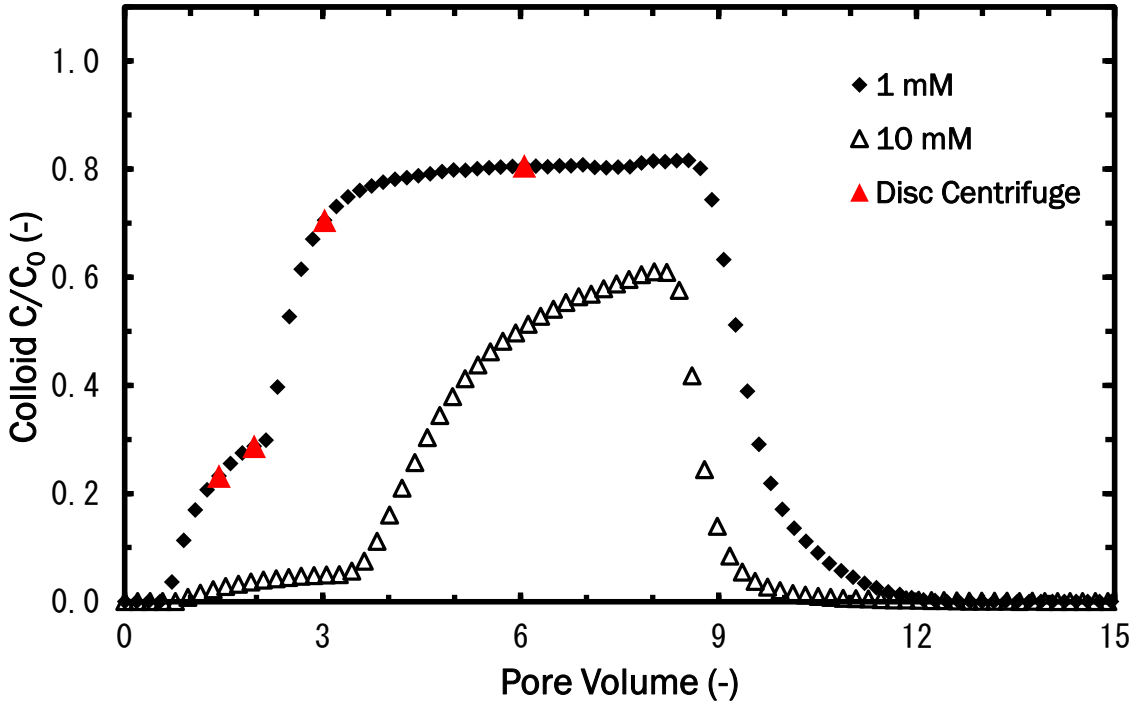

Figure 4.11: Observed BTCs of hollow SiO_2 NPs in 1 mM and 10 mM NaCl solution

Column transport tests on hollow particles showed peculiarly-shaped BTCs, characterized by a first plateau followed by a rapid increase in colloid breakthrough after approximately 2.5 to 3.5 PV: to the best of my knowledge, similar behaviours are not reported in literature. Disc centrifuge measurements were carried out to evaluate the possible influence of the micro-sized population on samples collected after 1.5, 2, 3 and 6 PV from initial injection (red triangles). Results are shown in *Figure 4.12*.

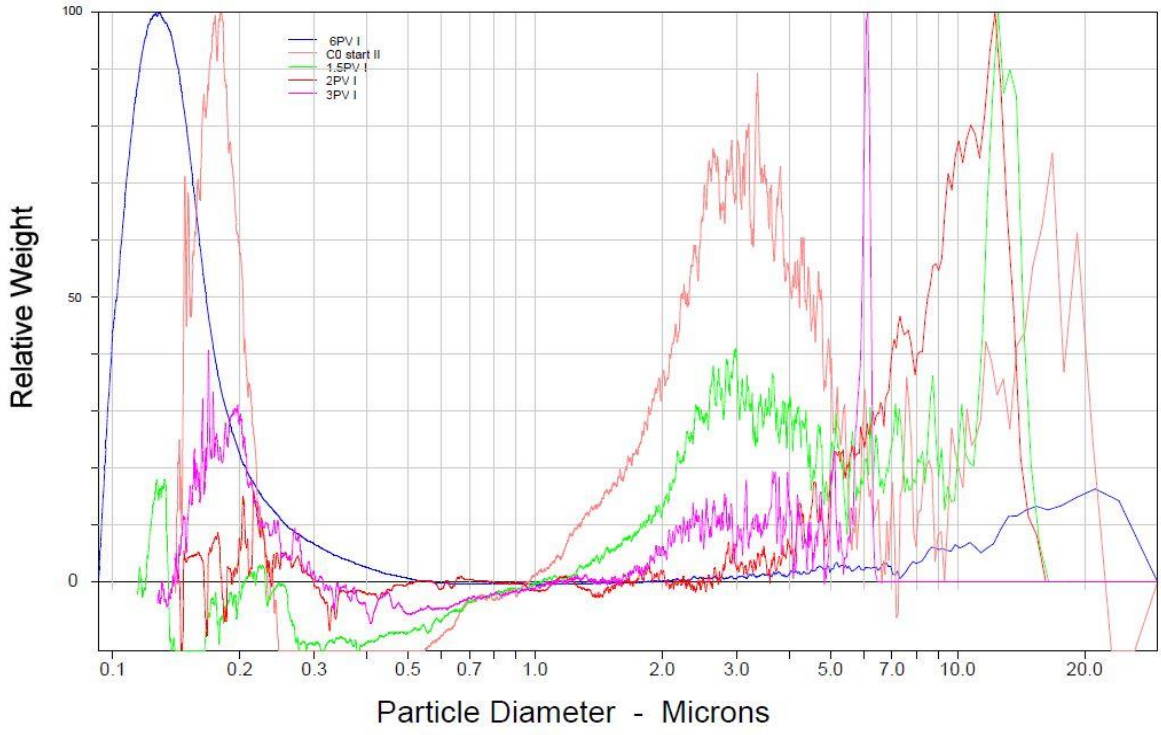

Figure 4.12: Disc centrifuge – hollow NPs' size distribution after 1.5, 2, 3 and 6 PV from injection

Disc centrifuge analysis revealed how micro-sized particles were the first to reach the outlet of the column, as size distributions of samples collected after 1.5 and 2 PV highlighted the exclusive presence of the micro-sized population. Size measurements at 3 and 6 PV, on the contrary, showed a significant reduction in the presence of the bigger population and a concomitant increase of small particles. This effect was probably due to the clogging of the porous medium that, in later stages of colloids deposition, acted as a mechanical filter towards the bigger population enabling the passage only of 250 nm-particles. Despite favourable attachment conditions (especially in 10 mM), significant transport of hollow particles occurred as a consequence of very low contact efficiency.

Particles' release was not promoted after post-flushing at reduced ionic strengths during tests conducted at 1 mM and 10 mM salt concentrations on both hollow and solid NPs: retained colloids were likely deposited irreversibly on primary minima, mechanically filtered or stuck in dead-end pores. Mass balance analysis provided further confirmation in that regard (*Table 4.5*).

Table 4.5: Recovered mass of hollow and solid SiO_2 NPs at 1 mM and 10 mM NaCl concentrations

I (mM)	Total recovered mass (%)	
	Solid NPs	Hollow NPs
1	90.0	73.5
10	91.5	33.0

Solid NPs mobility in high salinity conditions (100 mM and 1 M) was also assessed (*Figure 4.13* and *Figure 4.14*). At 100 mM, transport of solid particles showed significant differences from previous tests as even after 9 PV C/C_0 reached values of $\approx$ 0.9. The BTC also highlights significant NPs' release after the injection of 10 mM NaCl solution. The reversible deposition of solid SiO_2 NPs is likely to occur in a secondary well, as shown by DLVO interaction profile. Total recovered mass after post-flushing with deionized water amounted to 83.0%.

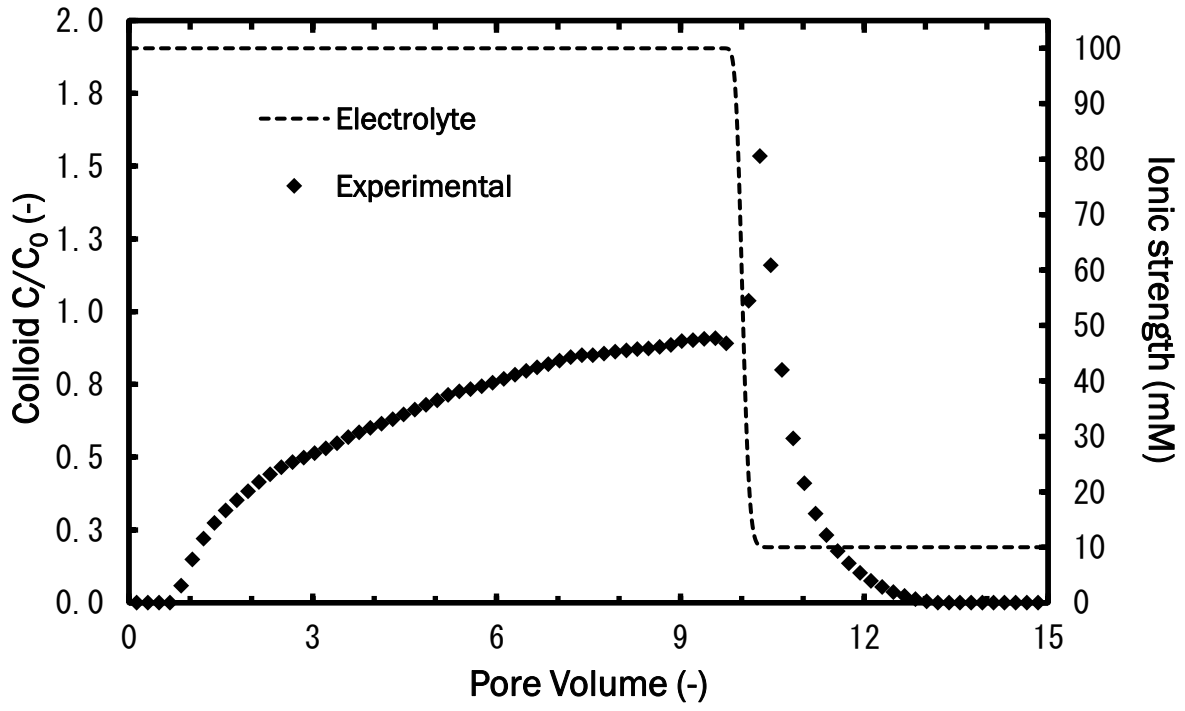

Figure 4.13: Observed BTC of solid SiO_2 NPs in transient ionic strength conditions (100 mM initial salt concentration)

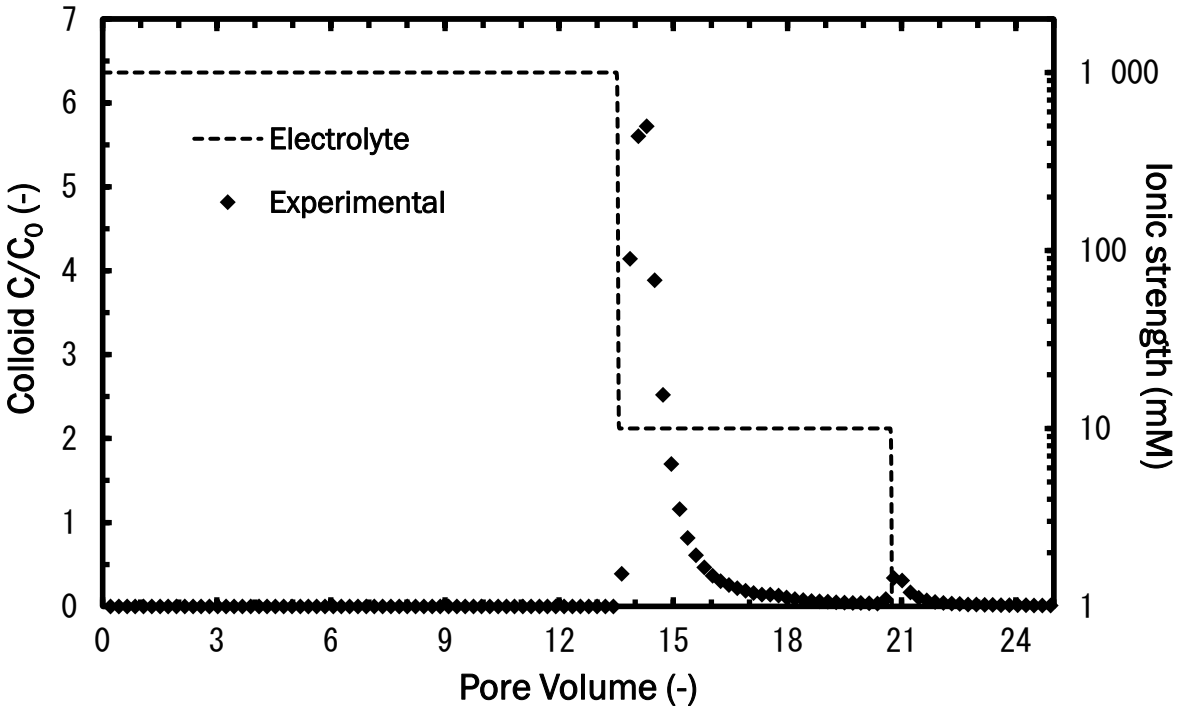

Figure 4.14: Observed BTC of solid SiO_2 NPs in transient ionic strength conditions (1M initial salt concentration)

In 1M ionic strength conditions, solid NPs were completely retained by the porous medium and no particles' breakthrough occurred until the injection of 10 mM NaCl solution. A similar behaviour was observed after a second post-flushing with decreased ionic strength (1 mM) that promoted further particles' release. After flushing the column with deionized water, 81.6% of injected particles were recovered. In 1M NaCl solution, solid NPs are expected to form weakly-bonded agglomerates as a result of attractive forces in the secondary minimum: agglomerates are likely to be filtered by the porous medium because of their increased size and are unable to reach the outlet of the column. When ionic strength decreases, repulsive sphere-sphere interactions arise and particles are re-mobilized. Only NPs very close to the grain surface remain irreversibly attached in the primary well.

4.3 Macro-scale modelling of experimental data

4.3.1 Tracer test

Tracer tests were carried out before every injection of silica NPs. Experimental data were least-squared fitted with equation (2.23) for estimation of hydrodynamic parameters (*Figure 4.15*).

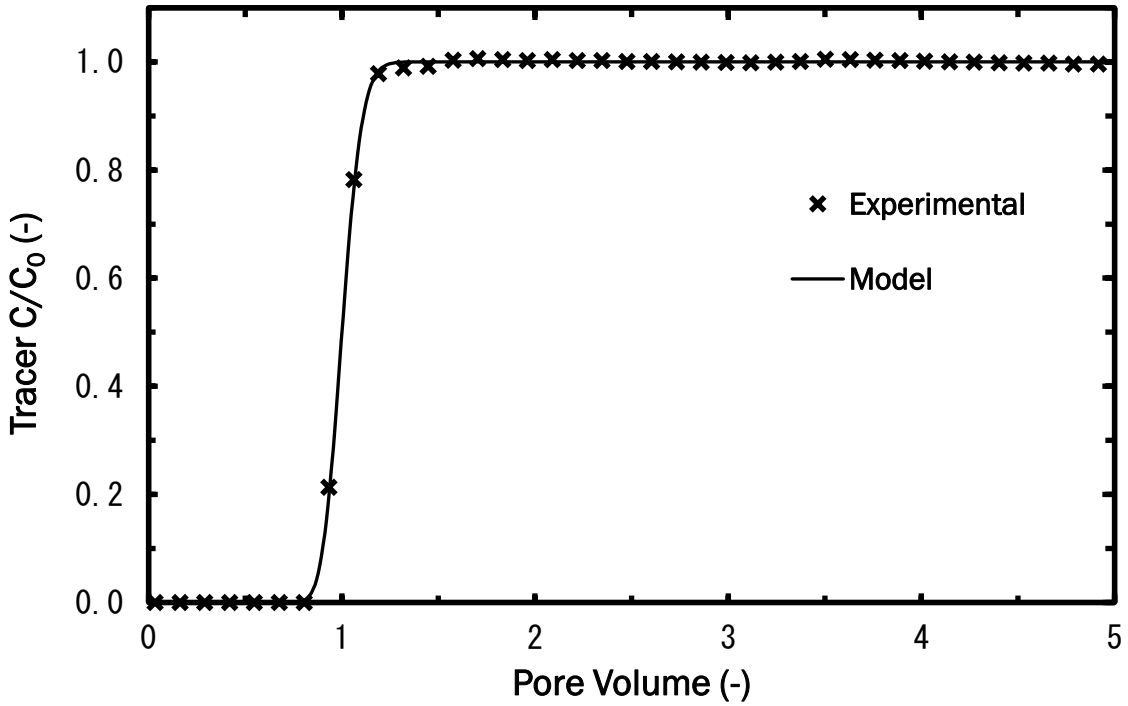

Figure 4.15: Example of observed and model-fitted BTC of NaCl

Average values of hydrodynamic parameters are reported in *Table 4.6*.

Table 4.6: Average estimated values of hydrodynamic parameters

α_x (mm)	1.011±0.42
n_e (-)	0.4043±0.028

4.3.2 Nanoparticles

Experimental particles' BTCs were modelled with Micro- and Nanoparticle transport, filtration and clogging Model- suite (MNMs, version 3.008), a numerical code developed at Politecnico di Torino. MNMs implements set of equations (2.29) in a Matlab environment using a finite-difference model [64]. Only features accounting for transport in 1D-geometry were employed.

Solid and hollow NPs' BTCs shown in paragraph 4.2 were fitted for the estimation of kinetic rates. CFT was found to be unable to model SiO_2 NPs BTCs: for the sake of brevity, simulations carried out under the clean bed filtration assumptions are not reported in this work. MFT was found to be better suited for colloids transport modelling.

Fitted BTCs of solid NPs at 1 mM and 10 mM electrolyte concentrations are reported in *Figure 4.16* and *Figure 4.17*. Both curves were fitted with one-active linear reversible site model: results show good approximation with experimental data. Since reduction in ionic strength didn't produce any particles' release, tests at 1 mM and 10 mM were not employed for the estimation of empirical coefficients $k_{a\infty}$, CDC, β_a, k_{d0}, CRC, β_d.

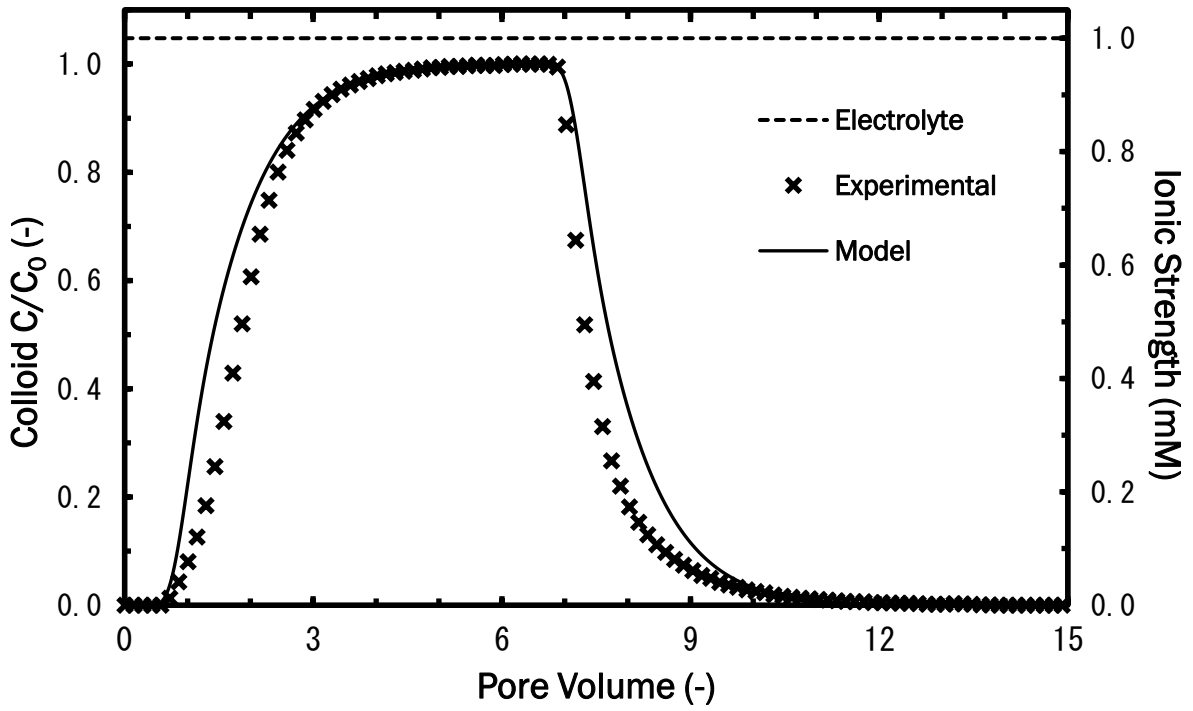

Figure 4.16: Observed and model-fitted BTC of solid SiO_2 NPs in 1 mM NaCl solution

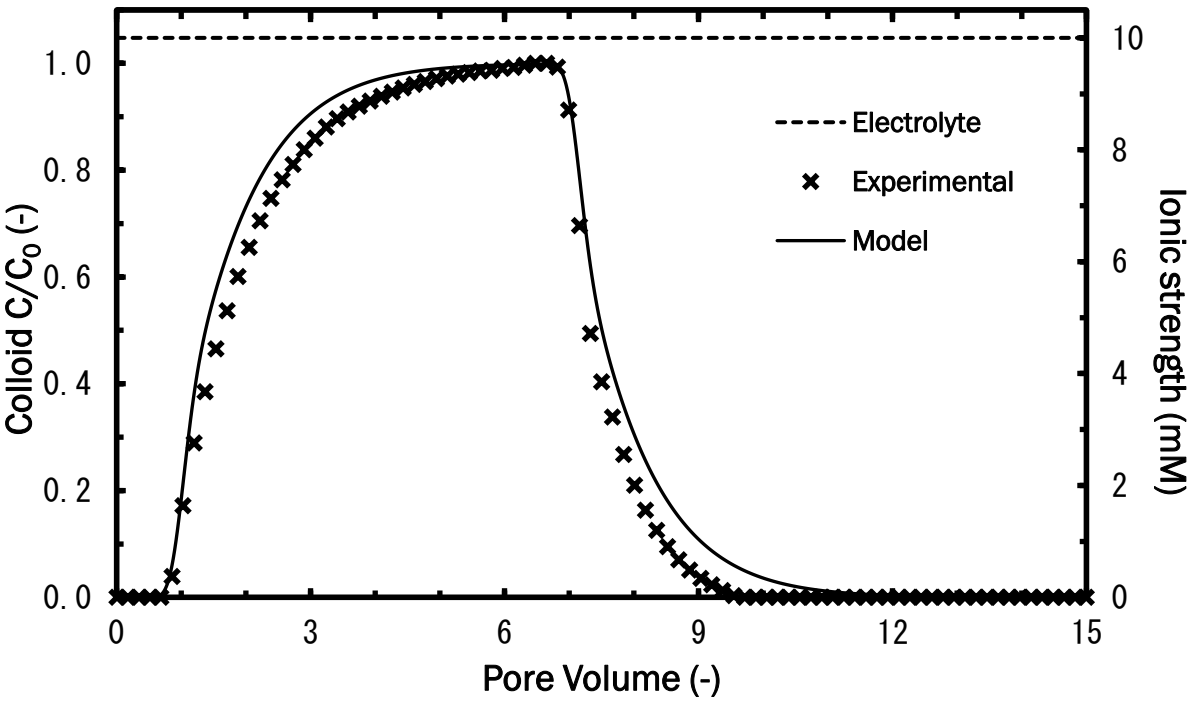

Figure 4.17: Observed and model-fitted BTC of solid SiO_2 NPs in 10 mM NaCl solution

Figure 4.18 shows the fitted BTC of solid NPs in transient ionic strength conditions (initial 100 mM NaCl solution): results are in good accordance with experimental data. A 1-active linear reversible site model was used for the estimation of empirical coefficients for transient ionic strength conditions ($k_{a\infty}$, CDC, β_a, k_{d0}, CRC, β_d).

Since no breakthrough occurred during the injection of solid NPs in 1M NaCl solution, no numerical solution was able to approximate the BTC reported in *Figure 4.14*.

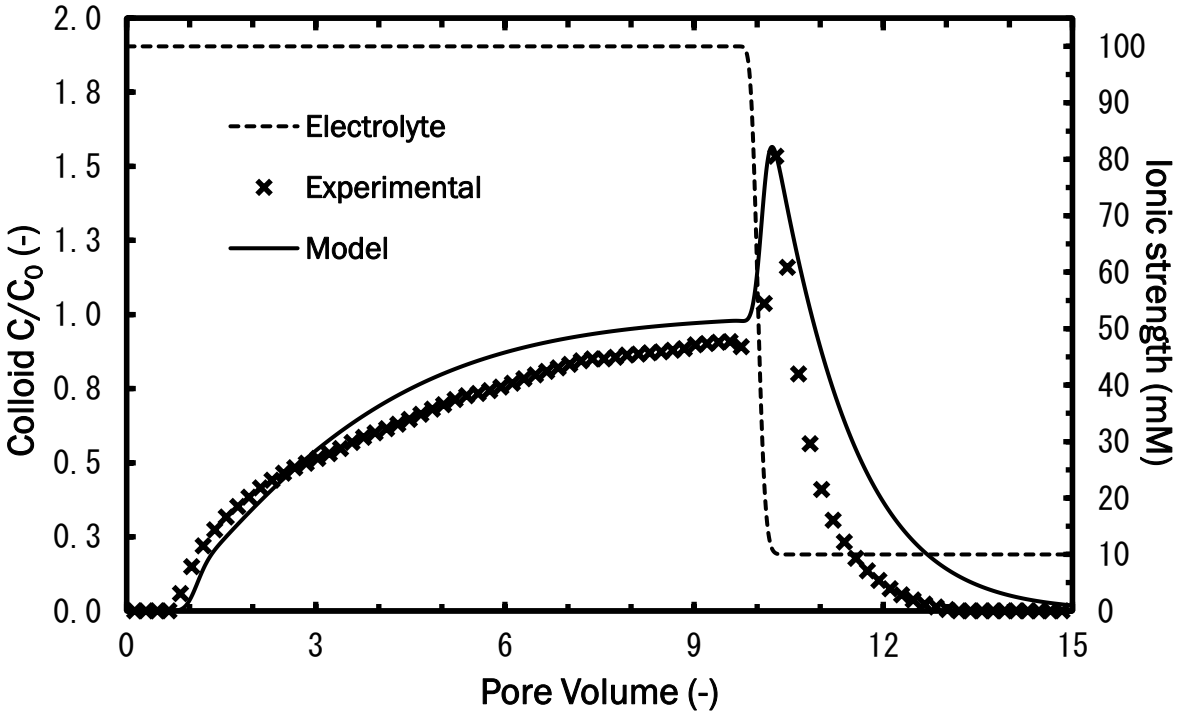

Figure 4.18: Observed and model-fitted BTC of solid SiO_2 NPs in transient ionic strength conditions

Estimated coefficients of colloid transport in transient solution chemistry are summarized in *Table 4.7*.

Table 4.7: Estimated coefficients of colloids transport in transient ionic strength

$k_{a\infty}$ (1/s)	CDC (mM)	β_a	k_{d0} (1/s)	CRC (mM)	β_d
2.51×10^{-2}	124	0.28	1.80×10^{-2}	12	0.41

Attachment and detachment rate in 1 mM and 10 mM NaCl solutions were calculated with equations (2.26) and (2.27) using estimated coefficients. These values were compared to those obtained by fitting of solid NPs' BTCs (as per *Figure 4.16* and *Figure 4.17*). Results are reported in *Table 4.8*.

Table 4.8: Comparison of fitted and calculated k_a and k_d values for 1-active site transport modelling of solid SiO_2 NPs

Initial I (mM)	Attachment rate k_a (1/s)		Detachment rate k_d (1/s)	
	Estimated	Calculated	Estimated	Calculated
1	6.14×10^{-3}	5.06×10^{-3}	9.99×10^{-3}	1.30×10^{-2}
10	6.15×10^{-3}	8.20×10^{-3}	9.57×10^{-3}	9.19×10^{-3}
100	/	1.21×10^{-2}	/	5.28×10^{-3}

Calculated kinetic rates compared well with fitted ones, suggesting a good accuracy in the estimation of empirical coefficients for transport in transient ionic strength conditions.

As expected from DLVO calculations and experimental BTCs, minimal difference was observed between kinetic rates obtained at 1 mM and 10 mM: estimated kinetic rates were consistent with data found in literature [20].

A similar approach was used to model the transport of hollow silica particles. In *Figure 4.19* the fitted BTC obtained at ionic strength equal to 1 mM is reported. Experimental data were fitted with a 2-active sites model (one linear reversible site and one linear irreversible) but a solution able to efficiently describe the "double-plateau" behaviour of hollow NPs BTC was not found.

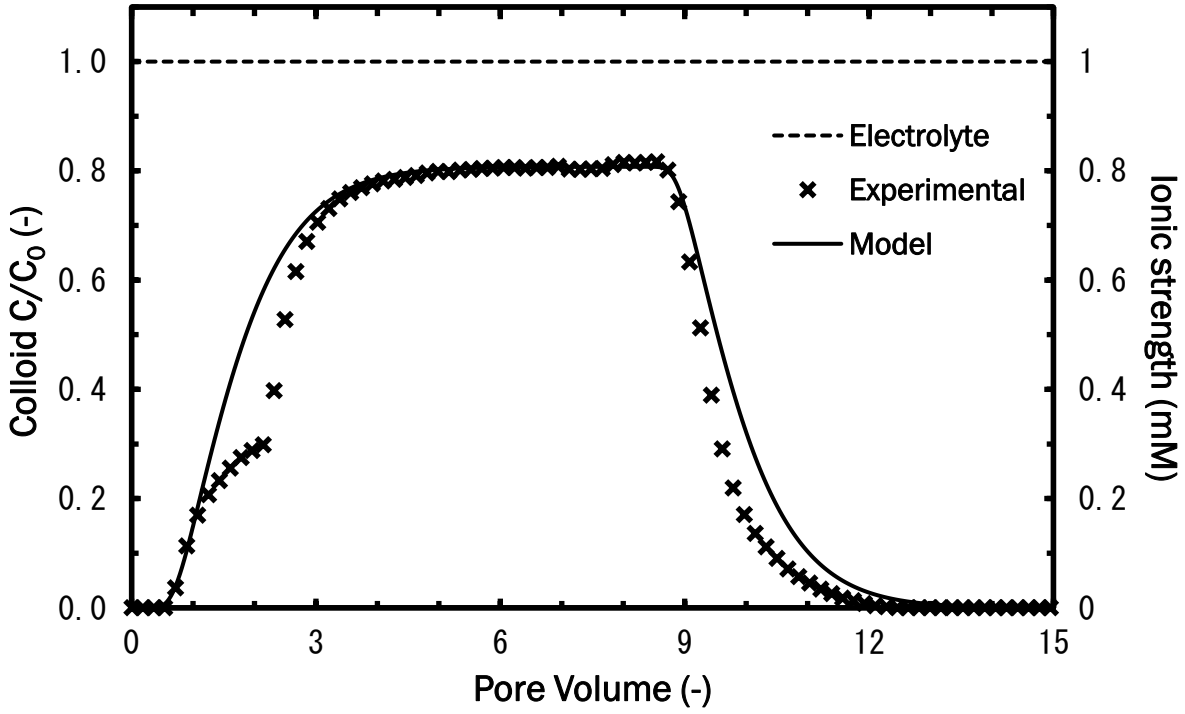

Figure 4.19: Observed and model-fitted BTC of hollow SiO_2 NPs in 1 mM NaCl solution

Worse results were observed after modelling hollow NPs transport at 10 mM salt concentration. A two-active sites model (one linear reversible site and one linear irreversible) was employed to fit experimental data. The least-squares fitting solution was found to be particularly unfit to reproduce measured concentrations, so a manual calibration attempting to model the kinetic interactions of the small population of hollow NPs was performed. Results are shown in *Figure 4.20*.

Estimated kinetic rates for hollow SiO_2 particles are summarized in *Table 4.9*.

Table 4.9: Estimated k_a and k_d values for 2-active sites transport modelling of hollow SiO_2 NPs

I (mM)	SITE 1		SITE 2	
	k_a (1/s)	k_d (1/s)	k_a (1/s)	k_d (1/s)
1	1.20×10^{-2}	1.61×10^{-2}	1.23×10^{-3}	0
10	2.95×10^{-2}	2.35×10^{-3}	3.15×10^{-3}	0

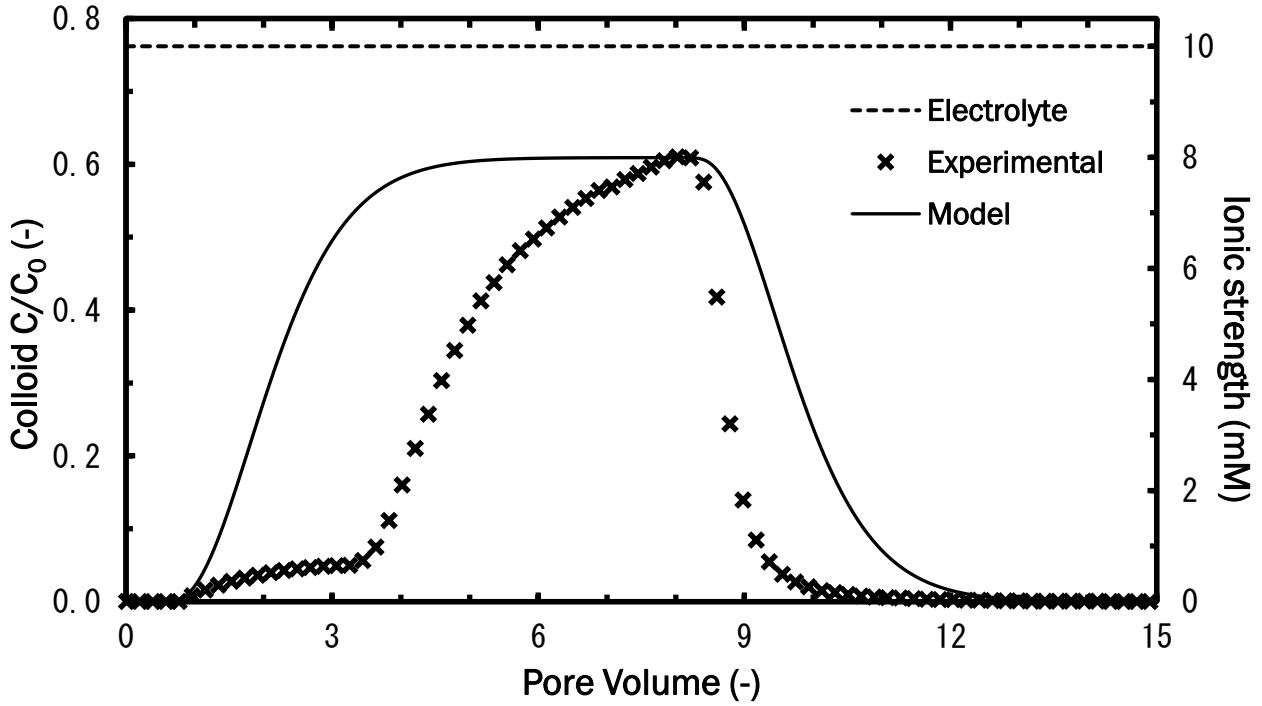

Figure 4.20: Observed and model-fitted BTC of hollow SiO_2 NPs in 10 mM NaCl solution

Despite the poor quality of the fitting, values of kinetic rates are consistent with DLVO profiles calculations, as increased ionic strength leads to an increase of attachment rates and a decrease of detachment rates.

5. Conclusions

In the frame of this work, two sets of solid and hollow silica nanoparticles were characterized in terms of size, morphology and surface properties and their behaviour in a lab-simulated groundwater environment was assessed. Due to their similar physical characteristics (e.g. density, Hamaker constant), solid particles were used as templates for mesoporous particles.

Stöber-synthesized solid SiO_2 NPs were found to be spherically-shaped with a diameter of 170 nm and a strongly charged surface (≈ -50 mV in 10 mM NaCl solution at natural pH). Commercial hollow SiO_2 NPs showed good sphericity, a weakly-charged surface (≈ -3 mV in 10 mM NaCl solution at natural pH) and a very disperse size distribution. In particular, two populations were proved to be relevant in determining hollow NPs behaviour in granular media: a "small" population with outer diameter of 250 nm and a 25nm-thick silica shell, and a "big" population formed of particles with sizes in the µ-range.

Both sets of particles showed good mobility in water-saturated granular media.

Solid NPs were able to reach the outlet of the column at high concentrations ($C/C_0 \approx 0.9$) even in high salinity conditions (100 mM) and their retention to sand grains was limited (17%). Only in extreme salinity conditions (1M) they were not transported, as aggregation in secondary minimum lead to particles' filtration by the porous medium.

Hollow NPs showed good mobility in sand-packed columns, consistently reaching values of normalized concentration beyond 0.6, even in favourable attachment conditions. These results were justified by the low value of single-collector contact efficiency in the conditions employed for the tests. Higher values of particles' mass retention were found for hollow NPs.

For all the transport tests carried out, DLVO and single collector contact efficiency calculations were found to be particularly accurate in describing SiO_2 particles behaviour.

Since discrepancies in experimental data between hollow and solid particles were mostly due to different surface properties. additional analysis were performed, assuming equal values zeta potentials, to understand possible intrinsic differences in the behaviour of hollow NPs in the environment. In particular, the influence of the inner sphere on DLVO interaction profiles and the effects of density and Hamaker constant on single collector contact efficiency were evaluated. Results revealed that the inner sphere can have a relevant influence on DLVO profiles only in extreme conditions (high a_{is}/a_p ratios, very small outer diameters), while density was proven to affect significantly single collector contact efficiencies only for big particles ($\eta_0(\mathrm{h}) \approx 0.61\,\eta_0(\mathrm{s})$ for a_p=10 µm). For the case in exam, differences in Hamaker constant were irrelevant with respect to single collector contact efficiency.

Calculations highlighted that, in typical conditions, hollow and solid particles' should behave very similarly.

MFT was used for macro-scale modelling of SiO_2 NPs transport. In particular, one-active linear reversible site model was used for interpretation of solid NPs BTCs, while a two-active sites model (one linear reversible site and one linear irreversible) was used for hollow NPs.

MFT was found to be well-suited to model solid NPs transport in porous media; estimated kinetic rates were consistent with data found in literature. Empirical equations correlating ionic strength with macro-

scale kinetic rates showed good results as calculated kinetic rates compared well with estimated rates obtained by fitting of BTCs.

Even accounting for multisite modelling, MFT was not able to accurately approximate the transport behaviour of hollow NPs, as the presence of the µ-sized population within commercial particles produced an “initial plateau” that no model was properly able to fit.

In conclusion, there is strong evidence that both sets of particles could behave as vectors for contaminants as they have shown good mobility in water-saturated porous media. Their use for environmental applications should be carefully evaluated, and regulatory decisions should be taken only after the assessment of transport of loaded particles. In choosing which type of particle is best suited to being introduced in the environment, priority should be given to the one that is best able to target a specific receptor.

Literature Cited

1. Einstein, A. Zur Theorie der Brownschen Bewegung. *Ann. Phys.* **324**, 371–381 (1906).

2. Commission Recommendation of 18 October 2011 on the definition of nanomaterialText with EEA relevance. 3

3. Klaine, S. J. *et al.* NANOMATERIALS IN THE ENVIRONMENT: BEHAVIOR, FATE, BIOAVAILABILITY, AND EFFECTS. *Environ. Toxicol. Chem.* **27**, 1825 (2008).

4. Kah, M. Nanopesticides and Nanofertilizers: Emerging Contaminants or Opportunities for Risk Mitigation? *Front. Chem.* **3**, (2015).

5. Kah, M. & Hofmann, T. Nanopesticide research: Current trends and future priorities. *Environ. Int.* **63**, 224–235 (2014).

6. Lövestam, G. *et al.* Considerations on a Definition of Nanomaterial for Regulatory Purposes. 40

7. Chemistry, I. U. of P. and A. IUPAC Gold Book - colloidal. doi:10.1351/goldbook.C01172

8. Perego, C., Bagatin, R., Tagliabue, M. & Vignola, R. Zeolites and related mesoporous materials for multi-talented environmental solutions. *Microporous Mesoporous Mater.* **166**, 37–49 (2013).

9. Walcarius, A. & Mercier, L. Mesoporous organosilica adsorbents: nanoengineered materials for removal of organic and inorganic pollutants. *J. Mater. Chem.* **20**, 4478 (2010).

10. Vance, M. E. *et al.* Nanotechnology in the real world: Redeveloping the nanomaterial consumer products inventory. *Beilstein J. Nanotechnol.* **6**, 1769–1780 (2015).

11. Inshakova, E. & Inshakov, O. World market for nanomaterials: structure and trends. *MATEC Web Conf.* **129**, 02013 (2017).

12. Slowing, I. I., Trewyn, B. G., Giri, S. & Lin, V. S.-Y. Mesoporous Silica Nanoparticles for Drug Delivery and Biosensing Applications. *Adv. Funct. Mater.* **17**, 1225–1236 (2007).

13. Kim, J. H. *et al.* Dye-sensitized nanocrystalline solar cells based on composite polymer electrolytes containing fumed silica nanoparticles. *Chem. Commun.* 1662 (2004). doi:10.1039/b405215c

14. Lehman, S. E. & Larsen, S. C. Zeolite and mesoporous silica nanomaterials: greener syntheses, environmental applications and biological toxicity. *Env. Sci Nano* **1**, 200–213 (2014).

15. Kah, M., Beulke, S., Tiede, K. & Hofmann, T. Nanopesticides: State of Knowledge, Environmental Fate, and Exposure Modeling. *Crit. Rev. Environ. Sci. Technol.* **43**, 1823–1867 (2013).

16. Liu, F. *et al.* Porous hollow silica nanoparticles as controlled delivery system for water-soluble pesticide. *Mater. Res. Bull.* **41**, 2268–2275 (2006).

17. Caruso, F. Nanoengineering of Inorganic and Hybrid Hollow Spheres by Colloidal Templating. *Science* **282**, 1111–1114 (1998).

18. Kim, I., Taghavy, A., DiCarlo, D. & Huh, C. Aggregation of silica nanoparticles and its impact on particle mobility under high-salinity conditions. *J. Pet. Sci. Eng.* **133**, 376–383 (2015).

19. Rauscher, H., Rasmussen, K. & Sokull-Klüttgen, B. Regulatory Aspects of Nanomaterials in the EU. *Chem. Ing. Tech.* **89**, 224–231 (2017).

20. Wang, C. *et al.* Retention and Transport of Silica Nanoparticles in Saturated Porous Media: Effect of Concentration and Particle Size. *Environ. Sci. Technol.* **46**, 7151–7158 (2012).

21. Petosa, A. R., Jaisi, D. P., Quevedo, I. R., Elimelech, M. & Tufenkji, N. Aggregation and Deposition of Engineered Nanomaterials in Aquatic Environments: Role of Physicochemical Interactions. *Environ. Sci. Technol.* **44**, 6532–6549 (2010).

22. Morris, J. & Willis, J. Nanotechnology White Paper. 137

23. Moore, M. N. Do nanoparticles present ecotoxicological risks for the health of the aquatic environment? *Environ. Int.* **32**, 967–976 (2006).

24. Vitorge, E., Szenknect, S., Martins, J. M. F. & Gaudet, J.-P. Size- and concentration-dependent deposition of fluorescent silica colloids in saturated sand columns: transport experiments and modeling. *Environ. Sci. Process. Impacts* **15**, 1590 (2013).

25. Yamashita, K. *et al.* Silica and titanium dioxide nanoparticles cause pregnancy complications in mice. *Nat. Nanotechnol.* **6**, 321–328 (2011).

26. Verwey, E. J. W. Theory of the Stability of Lyophobic Colloids. 6

27. Derjaguin, B. & Landau, L. Theory of the stability of strongly charged lyophobic sols and of the adhesion of strongly charged particles in solutions of electrolytes. *Prog. Surf. Sci.* **43**, 30–59 (1993).

28. de Vicente, J., Delgado, A. V., Plaza, R. C., Durán, J. D. G. & González-Caballero, F. Stability of Cobalt Ferrite Colloidal Particles. Effect of pH and Applied Magnetic Fields. *Langmuir* **16**, 7954–7961 (2000).

29. Ruckenstein, E. & Prieve, D. C. Adsorption and desorption of particles and their chromatographic separation. *AIChE J.* **22**, 276–283 (1976).

30. Phenrat, T., Liu, Y., Tilton, R. D. & Lowry, G. V. Adsorbed Polyelectrolyte Coatings Decrease Fe ^{0} Nanoparticle Reactivity with TCE in Water: Conceptual Model and Mechanisms. *Environ. Sci. Technol.* **43**, 1507–1514 (2009).

31. Chen, Z. H. *et al.* Characterizing Size and Porosity of Hollow Nanoparticles: SAXS, SANS, TEM, DLS, and Adsorption Isotherms Compared. *Langmuir* **28**, 15350–15361 (2012).

32. Hogg, R., Healy, T. W. & Fuerstenau, D. W. Mutual coagulation of colloidal dispersions. *Trans. Faraday Soc.* **62**, 1638 (1966).

33. Gregory, J. Approximate expressions for retarded van der waals interaction. *J. Colloid Interface Sci.* **83**, 138–145 (1981).

34. Lipkin, D. M., Israelachvili, J. N. & Clarke, D. R. Estimating the metal-ceramic van der Waals adhesion energy. *Philos. Mag. A* **76**, 715–728 (1997).

35. Shen, C. *et al.* DLVO Interaction Energies for Hollow Particles: The Filling Matters. *Langmuir* **34**, 12764–12775 (2018).

36. Shen, C. *et al.* DLVO Interaction Energies between Hollow Spherical Particles and Collector Surfaces. *Langmuir* **33**, 10455–10467 (2017).

37. Bhattacharjee, S. DLS and zeta potential – What they are and what they are not? *J. Controlled Release* **235**, 337–351 (2016).

38. Gregory, J. Interaction of unequal double layers at constant charge. *J. Colloid Interface Sci.* **51**, 44–51 (1975).

39. Dunphy Guzman, K. A., Finnegan, M. P. & Banfield, J. F. Influence of Surface Potential on Aggregation and Transport of Titania Nanoparticles. *Environ. Sci. Technol.* **40**, 7688–7693 (2006).

40. Yao, K.-M., Habibian, M. T. & O'Melia, C. R. Water and waste water filtration. Concepts and applications. *Environ. Sci. Technol.* **5**, 1105–1112 (1971).

41. Tufenkji, N. & Elimelech, M. Correlation Equation for Predicting Single-Collector Efficiency in Physicochemical Filtration in Saturated Porous Media. *Environ. Sci. Technol.* **38**, 529–536 (2004).

42. Nelson, K. E. & Ginn, T. R. Colloid Filtration Theory and the Happel Sphere-in-Cell Model Revisited with Direct Numerical Simulation of Colloids. *Langmuir* **21**, 2173–2184 (2005).

43. Messina, F., Marchisio, D. L. & Sethi, R. An extended and total flux normalized correlation equation for predicting single-collector efficiency. *J. Colloid Interface Sci.* **446**, 185–193 (2015).

44. Happel, J. Viscous flow in multiparticle systems: Slow motion of fluids relative to beds of spherical particles. *AIChE J.* **4**, 197–201 (1958).

45. Ma, H., Pedel, J., Fife, P. & Johnson, W. P. Hemispheres-in-Cell Geometry to Predict Colloid Deposition in Porous Media. *Environ. Sci. Technol.* **43**, 8573–8579 (2009).

46. Rajagopalan, R. & Tien, C. Trajectory analysis of deep-bed filtration with the sphere-in-cell porous media model. *AIChE J.* **22**, 523–533 (1976).

47. Nelson, K. E. & Ginn, T. R. New collector efficiency equation for colloid filtration in both natural and engineered flow conditions: NEW COLLECTOR EFFICIENCY EQUATION FOR COLLOID. *Water Resour. Res.* **47**, (2011).

48. Ma, H., Hradisky, M. & Johnson, W. P. Extending Applicability of Correlation Equations to Predict Colloidal Retention in Porous Media at Low Fluid Velocity. *Environ. Sci. Technol.* **47**, 2272–2278 (2013).

49. Molfetta, A. & Sethi, R. *Ingegneria degli acquiferi*. (Springer Milan, 2012). doi:10.1007/978-88-470-1851-8

50. Fel, L. & Bear, J. Dispersion and Dispersivity Tensors in Saturated Porous Media with Uniaxial Symmetry. *Transp. Porous Media* **85**, 259–268 (2010).

51. Tiraferri, A., Tosco, T. & Sethi, R. Transport and retention of microparticles in packed sand columns at low and intermediate ionic strengths: experiments and mathematical modeling. *Environ. Earth Sci.* **63**, 847–859 (2011).

52. Bianco, C. Modeling of the injection and long term fate of nanoparticles in groundwater systems. 153

53. Ogata, A. & Banks, R. B. A Solution of the Differential Equation of Longitudinal Dispersion in Porous Media. 18

54. Tosco, T. & Sethi, R. Transport of Non-Newtonian Suspensions of Highly Concentrated Micro- And Nanoscale Iron Particles in Porous Media: A Modeling Approach. *Environ. Sci. Technol.* **44**, 9062–9068 (2010).

55. Logan, B. E., Jewett, D. G., Arnold, R. G., Bouwer, E. J. & O'Melia, C. R. Clarification of Clean-Bed Filtration Models. *J. Environ. Eng.* **121**, 869–873 (1995).

56. Logan, B. E., Jewett, D. G., Arnold, R. G., Bouwer, E. J. & O'Melia, C. R. Closure to "Clarification of Clean-Bed Filtration Models" by B. E. Logan, D. G. Jewett, R. G. Arnold, E. J. Bouwer, and C. R. O'Melia. *J. Environ. Eng.* **123**, 730–731 (1997).

57. Bradford, S. A., Yates, S. R., Bettahar, M. & Simunek, J. Physical factors affecting the transport and fate of colloids in saturated porous media: FACTORS AFFECTING THE FATE OF COLLOIDS. *Water Resour. Res.* **38**, 63-1-63–12 (2002).

58. Bradford, S. A., Simunek, J., Bettahar, M., van Genuchten, M. T. & Yates, S. R. Modeling Colloid Attachment, Straining, and Exclusion in Saturated Porous Media. *Environ. Sci. Technol.* **37**, 2242–2250 (2003).

59. Tschapek, M., Falasca, S. & Wasowski, C. Quartz sand: Apparent hydroxylation – dehydroxylation and ζ-potential. *Z. Für Pflanzenernähr. Bodenkd.* **149**, 728–734 (1986).

60. Berg, J. M., Romoser, A., Banerjee, N., Zebda, R. & Sayes, C. M. The relationship between pH and zeta potential of ~ 30 nm metal oxide nanoparticle suspensions relevant to *in vitro* toxicological evaluations. *Nanotoxicology* **3**, 276–283 (2009).

61. Antonio Alves Júnior, J. & Baptista Baldo, J. The Behavior of Zeta Potential of Silica Suspensions. *New J. Glass Ceram.* **04**, 29–37 (2014).

62. Tosco, T., Tiraferri, A. & Sethi, R. Ionic Strength Dependent Transport of Microparticles in Saturated Porous Media: Modeling Mobilization and Immobilization Phenomena under Transient Chemical Conditions. *Environ. Sci. Technol.* **43**, 4425–4431 (2009).

63. Lenhart, J. J. & Saiers, J. E. Colloid Mobilization in Water-Saturated Porous Media under Transient Chemical Conditions. *Environ. Sci. Technol.* **37**, 2780–2787 (2003).

64. Tosco, T. & Sethi, R. MNM1D: A Numerical Code for Colloid Transport in Porous Media: Implementation and Validation. *Am. J. Environ. Sci.* **5**, 516–524 (2009).

65. Torkzaban, S., Wan, J., Tokunaga, T. K. & Bradford, S. A. Impacts of bridging complexation on the transport of surface-modified nanoparticles in saturated sand. *J. Contam. Hydrol.* **136–137**, 86–95 (2012).

66. Hunter, R. J. The Calculation of Zeta Potential. in *Zeta Potential in Colloid Science* 59–124 (Elsevier, 1981). doi:10.1016/B978-0-12-361961-7.50007-9

67. Zafeiropoulos, N. E. *Interface Engineering of Natural Fibre Composites for Maximum Performance*. (Elsevier, 2011).

68. Elimelech, M., Nagai, M., Ko, C.-H. & Ryan, J. N. Relative Insignificance of Mineral Grain Zeta Potential to Colloid Transport in Geochemically Heterogeneous Porous Media. *Environ. Sci. Technol.* **34**, 2143–2148 (2000).

69. Fujita, Y. & Kobayashi, M. Transport of colloidal silica in unsaturated sand: Effect of charging properties of sand and silica particles. *Chemosphere* **154**, 179–186 (2016).

70. Stöber, W., Fink, A. & Bohn, E. Controlled growth of monodisperse silica spheres in the micron size range. *J. Colloid Interface Sci.* **26**, 62–69 (1968).

71. Rogošić, M., Mencer, H. J. & Gomzi, Z. Polydispersity index and molecular weight distributions of polymers. *Eur. Polym. J.* **32**, 1337–1344 (1996).

72. Häggmark, C. & Königsson, S. Rheological Characterization of Solids Phase in Biomass Processes of Disc-Stack Centrifuges. *Chem. Eng. Technol.* **41**, 2289–2297 (2018).

73. Lewis, J. & Sjöstrom, J. Optimizing the experimental design of soil columns in saturated and unsaturated transport experiments. *J. Contam. Hydrol.* **115**, 1–13 (2010).

74. Barbosa-García, O. *et al.* UV–vis absorption spectroscopy and multivariate analysis as a method to discriminate tequila. *Spectrochim. Acta. A. Mol. Biomol. Spectrosc.* **66**, 129–134 (2007).

75. Rocha, F. S., Gomes, A. J., Lunardi, C. N., Kaliaguine, S. & Patience, G. S. Experimental methods in chemical engineering: Ultraviolet visible spectroscopy-UV-Vis. *Can. J. Chem. Eng.* **96**, 2512–2517 (2018).

76. Rodríguez-de Marcos, L. V., Larruquert, J. I., Méndez, J. A. & Aznárez, J. A. Self-consistent optical constants of SiO_2 and Ta_2O_5 films. *Opt. Mater. Express* **6**, 3622 (2016).